12 May 2025

Establishing the Compatibility of Anolytes and Catholytes in Dual Electrolyte Solid-State Batteries

Tyler Pennebaker[1], Elias Sebti[1], Abhishek Panchal[2,3], Chen-Jui Huang[4], Yulia Trenikhina[5], Tianyu Li[1], Yan Li[3], Yuheng Li[3], Stephen Kelly[5], Ying Shirley Meng[4,6,7], Pieremanuele Canepa[2], Raphaële Clément[1]

1. University of California, Santa Barbara
2. University of Houston
3. National University of Singapore
4. University of Chicago
5. Zeiss Research Microscopy Solutions
6. University of California, San Diego
7. Argonne National Laboratory

Abstract

In the pursuit of long-lasting, high-energy density solid-state batteries, dual solid electrolyte designs offer a unique path toward stabilizing the electrode-electrolyte in- terfaces in the presence of a high-voltage positive electrode and a low-voltage negative electrode. However, electrolyte pairings that form a stable interface under battery operating conditions must be identified. In this study, we used the onset reaction tem- perature as a proxy to assess the chemical compatibility between a chloride (Li2ZrCl6 (LZC))catholyte(ahighoxidativestabilityelectrolyte)andtwocommonthiophosphate (Li3PS4 (LPS) and Li6PS5Cl (LPSC)) anolytes (high reductive stability electrolytes). While LPS reacts with LZC starting at 90°C, the LZC–LPSC pairing appears sta- ble up to 260°C. When heated to 300°C, the two pairings decompose to form LiCl, a layered LixZryP2S6 phase, ZrS2, ZrS3, S8, as well as γ−Li3PS4 for the LZC–LPSC pairing. Consistent with those findings, first-principles calculations show that neither pairing is thermodynamically stable. However, a higher decomposition energy is pre- dicted for the LZC–LPSC combination, suggesting that it is kinetically stabilized up to 260°C. The LZC–LPSC interface is conductive to Li-ions, with an extremely low resis- tance (4.2 Ω cm−2). Furthermore, cells comprising an LZC–LPSC bilayer separating a LiNi0.8Mn0.1Co0.1O2 positive electrode and Li-In negative electrode exhibit exception- ally stable performance, with 90.0 % and 83.8 % of their initial capacity retained after 200 and 500 cycles, respectively. These findings allow us to propose several criteria for designing stable electrified interfaces for a wide range of electrochemical devices.

Keywords

Solid-state batteries, Interfaces, Reactivity, Dual electrolyte, Ion transport

Establishing the Compatibility of Anolytes and Catholytes in Dual Electrolyte Solid-State Batteries

Tyler N.T. Pennebaker,[†,‡,▽] Elias Sebti,[†,‡,▽] Abhishek Panchal,[¶,§,‖] Chen-Jui Huang,[⊥] Yulia Trenikhina,[#] Tianyu Li,[†,‡] Yan Li,[‖] Yuheng Li,[‖] Stephen T. Kelly,[#] Y. Shirley Meng,[@,⊥,△] Pieremanuele Canepa,[*,¶,§] and Raphaële J. Clément[*,†,‡]

†Materials Department, University of California Santa Barbara, Santa Barbara, California 93106, United States

‡Materials Research Laboratory, University of California Santa Barbara, Santa Barbara, California 93106, United States

¶Department of Electrical and Computer Engineering, University of Houston, Houston, Texas, 77204, United States

§Texas Center for Superconductivity, University of Houston, Houston, Texas, 77204, United States

‖Department of Materials Science and Engineering, National University of Singapore, 9 Engineering Drive 1, 117575, Singapore

⊥Pritzker School of Molecular Engineering, University of Chicago, Chicago, Illinois 60637, United States

#Zeiss Research Microscopy Solutions, Carl Zeiss X-ray Microscopy, Dublin, California 94568, United States

@Materials Science and Engineering Program, University of California San Diego, La Jolla, 92093, United States

△Energy Storage Research Alliance, Argonne National Laboratory, Lemont, Illinois 60439, United States

▽Contributed equally to this work

E-mail: pcanepa@central.uh.edu; rclement@ucsb.edu

Abstract

In the pursuit of long-lasting, high-energy density solid-state batteries, dual solid electrolyte designs offer a unique path toward stabilizing the electrode-electrolyte interfaces in the presence of a high-voltage positive electrode and a low-voltage negative electrode. However, electrolyte pairings that form a stable interface under battery operating conditions must be identified. In this study, we used the onset reaction temperature as a proxy to assess the chemical compatibility between a chloride (Li_2ZrCl_6 (LZC)) catholyte (a high oxidative stability electrolyte) and two common thiophosphate (Li_3PS_4 (LPS) and Li_6PS_5Cl (LPSC)) anolytes (high reductive stability electrolytes). While LPS reacts with LZC starting at 90 °C, the LZC–LPSC pairing appears stable up to 260 °C. When heated to 300 °C, the two pairings decompose to form LiCl, a layered $Li_xZr_yP_2S_6$ phase, ZrS_2, ZrS_3, S_8, as well as γ–Li_3PS_4 for the LZC–LPSC pairing. Consistent with those findings, first-principles calculations show that neither pairing is thermodynamically stable. However, a higher decomposition energy is predicted for the LZC–LPSC combination, suggesting that it is kinetically stabilized up to 260 °C. The LZC–LPSC interface is conductive to Li-ions, with an extremely low resistance ($4.2\,\Omega\,cm^{-2}$). Furthermore, cells comprising an LZC–LPSC bilayer separating a $LiNi_{0.8}Mn_{0.1}Co_{0.1}O_2$ positive electrode and Li-In negative electrode exhibit exceptionally stable performance, with 90.0 % and 83.8 % of their initial capacity retained after 200 and 500 cycles, respectively. These findings allow us to propose several criteria for designing stable electrified interfaces for a wide range of electrochemical devices.

1 Introduction

Given the continued upward trend in global anthropogenic greenhouse gas emissions, there is a pressing need to electrify transportation. Increasing electric vehicle adoption hinges on further developing Li-ion batteries to reduce cost, increase their energy density, and improve

their rate capability, durability, and safety. Solid-state batteries (SSBs) that comprise an inorganic solid electrolyte to shuttle Li^+ ions between the two electrodes could potentially lead to improvements in all areas. Indeed, SSBs open the door for increased packing efficiency at the cell module level by using bipolar stack architectures that decrease the amount of packaging required.[1] Unlike standard liquid electrolytes, inorganic solid electrolytes are single-ion conductors, whereby all current is carried by the mobile Li^+ ions or their vacancies. Hence, these materials hold promise for reducing polarization in the electrolyte bulk and improving rate performance.[2,3] In addition, inorganic solid electrolytes are significantly less flammable than the organic electrolytes used in currently commercialized cells, offering a significant safety advantage.

Stable long-term cycling of a high-voltage SSB requires the solid electrolyte to be electrochemically stable over a wide voltage window that spans both the oxidative potentials at the interface with the positive electrode and the reducing potentials at the negative electrode interface. Degradation of the solid electrolyte at either interface can lead to the formation of insulating interphases, impede Li^+ transport across the cell, and reduce its capacity and energy density. Importantly, increased resistance at the electrode-electrolyte interface can result in current heterogeneities, inhomogeneous Li plating or intercalation, dendrite nucleation and growth, and mechanical degradation through delamination and cracking, compromising the battery's cycle life.[4–7] Unfortunately, no known solid electrolyte chemistry combines high chemical and electrochemical stability, high Li-ion conductivity, and good processability. For example, sulfide and thiophosphate electrolytes offer liquid-like ionic conductivities, good processability, and even passivating interfaces against Li metal but degrade above 2.3 V vs. Li/Li^+, especially in the presence of conductive additives in the composite cathode.[8–21] Oxide-based electrolytes offer superior electrochemical stability compared to sulfides and thiophosphates, and conductivities up to 5 mS cm^{-1}, but at the expense of processability, as they need to be sintered with the positive electrode material to

facilitate grain boundary conduction.[22–26] Chloride-based electrolytes exhibit ionic conductivities on the order of mS cm^{-1} and tend to be stable at high potentials (> 4 V vs. Li/Li^+), but form mixed conductive interphases against Li metal that impede Li^+ conduction and lead to continuous performance degradation.[27–40]

A path towards scalable, high-energy-density SSBs can be imagined by harnessing two solid electrolytes with high ionic conductivities and differing electrochemical stability ranges. An electrolyte with a high oxidative stability is used as the catholyte in the composite cathode, and a single layer of a second solid electrolyte with good reductive stability (the anolyte) separates the negative electrode and the composite cathode. In this architecture, the catholyte ensures stable interfaces with the positive electrode active material and conductive additive, and the anolyte layer forms a stable interface with the negative electrode. This "single-layer" approach has been demonstrated in various Li- and Na-based SSBs combining a halide catholyte and thiophosphate anolyte.[40–47] An additional layer of the catholyte can be inserted between the anolyte and the cathode composite to avoid any possible contact between the cathode active material (and conductive additive) and the anolyte. Several studies have shown that this "bilayer" architecture drastically reduces reactivity and impedance growth at all electrode-electrolyte interfaces.[38,39,44–64] However, few studies have investigated the chemical stability and ion transport properties of the additional interface between the catholyte and anolyte in such architectures.

Rosenbach et al. employed a bilayer approach that combined Li_3InCl_6 (LIC) and Li_6PS_5Cl (LPSC) in a $LiNi_{0.8}Mn_{0.1}Co_{0.1}O_2$+LIC|LIC|LPSC|Li-In cell and identified the formation of an interfacial region between the two electrolytes rich in In and S, resulting in significant impedance build-up and rapid capacity loss during cycling.[44] Inspired by this work, we further explored the chemical decomposition of LIC in contact with LPSC by subjecting mixed LIC–LPSC pellets to increasing heat treatment temperatures. Although no reactivity was observed upon mixing the two electrolytes at room temperature, reaction products

were observed after heat treatments as low as 70 °C (see Figure S1), suggesting that the LIC–LPSC interface is reactive, in good agreement with Rosenbach et al. Clearly, a better understanding of the compatibility of contrasting solid electrolyte chemistries is needed. In addition, these preliminary results suggest that a simple heat treatment strategy may be effective in identifying chemically compatible solid electrolyte pairings.

This work assesses the compatibility of a chloride catholyte with two thiophosphate anolytes using a joint experimental and computational approach. We chose Li_2ZrCl_6 (LZC) as the catholyte because chlorides are generally stable up to high potentials[28,40] and have demonstrated sufficiently high ionic conductivities for practical applications.[31–39,48] Additionally, LZC is stable in contact with the $LiNi_{0.8}Mn_{0.1}Co_{0.1}O_2$ (NMC811) positive electrode,[55] and Zr is non-toxic and benefits from a reliable supply chain.[65] We compared Li_3PS_4 (LPS) and argyrodite Li_6PS_5Cl (LPSC) as anolytes. While the latter forms a passivating interface with Li metal,[13,66] the former shows a lower conductivity and reacts with Li metal and Li-In anodes and is therefore less attractive for SSB applications.

We hypothesize that the onset temperature for the reaction between two solid electrolytes can serve as a proxy for their compatibility in a dual-electrolyte SSB. The onset reaction temperature for the LZC–LPS and LZC–LPSC pairings was determined to be ca. 90 °C and 260 °C, respectively, from *in situ* heating synchrotron X-ray diffraction (XRD) results. The decomposition products were identified from examination of mixed LZC–LPS and LZC–LPSC pellets heat treated up to 300 °C, using XRD, solid-state nuclear magnetic resonance (ssNMR), X-ray photoelectron spectroscopy, and Raman spectroscopy. The two pairings decompose to form LiCl, a layered $Li_xZr_yP_2S_6$ phase, ZrS_2, ZrS_3, S_8, as well as γ–Li_3PS_4 for the LZC–LPSC pairing. Although first-principles density functional theory calculations predict that neither the LZC–LPS nor the LZC–LPSC pairing is thermodynamically stable, consistent with experimental findings, they also suggest more favorable decomposition pathways for LZC in contact with LPSC than with LPS, contrary to our observations. This

discrepancy indicates that sluggish reaction kinetics are responsible for the observed stability of the LZC–LPSC system up to 260 °C. Rapid Li-ion transport between the LZC and LPSC phases is evidenced by NMR, and a remarkably low interfacial resistance of $4.2\,\Omega\,cm^{-2}$ is determined by electrochemical impedance spectroscopy, accounting for only 1.5 % of the total resistance of a sandwich LPSC–LZC–LPSC pellet. The electrochemical performance of LZC–LPSC dual-electrolyte SSBs comprising a $LiNi_{0.8}Mn_{0.1}Co_{0.1}O_2$ (NMC811) positive electrode and a Li-In negative electrode was evaluated in single-layer and bilayer configurations. While single-layer cells show an average 63.0 % capacity retention after 200 cycles at 30 °C, bilayer cells show an impressive 90.0 % and 83.8 % average capacity retention after 200 and 500 cycles, respectively. Overall, this work reveals that the Li_2ZrCl_6–Li_6PS_5Cl system is a promising solid electrolyte pairing for SSBs comprising a high-voltage oxide cathode and a low-voltage metallic anode. These results further provide new avenues towards the design of stable electrified interfaces for use in energy-dense SSBs and a wide range of electrochemical devices.

2 Results and Discussion

2.1 Monitoring chemical reactivity between chloride and thiophosphate solid electrolytes

2.1.1 Onset reaction temperature as a proxy for solid electrolyte compatibility

The onset temperature of the reaction between two compounds depends on the reaction's thermodynamic driving force and activation energy barrier. As such, the onset temperature of the reaction between two solid electrolytes can provide key insight into their chemical compatibility and can be used to identify electrolyte pairings that form a stable interface within a dual-electrolyte cell during electrochemical cycling, assuming that the solid electrolytes are

sufficiently electronically insulating.

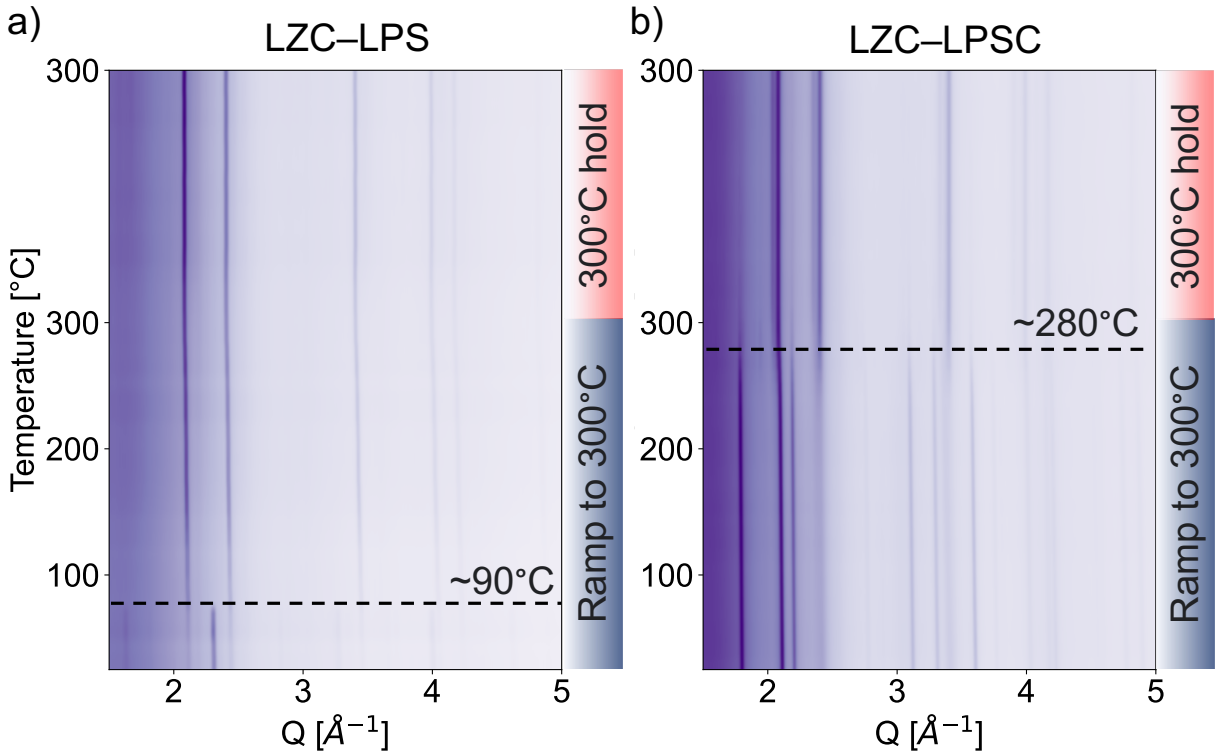

Figure 1: Contour plot representation of diffraction patterns collected on as-prepared/as-received a) LZC–LPS and b) LZC–LPSC mixed powder samples during a temperature ramp from room temperature to 300 °C, followed by a 20 minute hold at 300 °C.

The onset temperature of the reaction between Li_2ZrCl_6 (LZC) and either Li_3PS_4 (LPS) or Li_6PS_5Cl (LPSC) was determined from *in situ* heating synchrotron X-ray diffraction (sXRD) experiments on mixtures of as-prepared or as-received powders. LZC was synthesized via ball milling using a reported procedure,[40] and LPS and LPSC were purchased from NEI Corporation. Structural characterization of the three solid electrolytes using XRD and ^{6}Li and ^{3}1P solid-state NMR (ssNMR) is presented in Figures S3, S5, and S7. The electrolytes were phase-pure from XRD, with a small amount of LiCl impurity in the LZC sample detected by ^{6}Li ssNMR. LZC adopts a trigonal $P\bar{3}m1$ structure, LPS an orthorhombic *Pnma* structure (β phase), and LPSC a cubic $F\bar{4}3m$ structure. The synchrotron XRD

patterns obtained during *in situ* heating are presented in Figure 1. Over the course of a temperature ramp from room temperature to 300 °C, both solid electrolyte mixtures react to form LiCl. The LZC–LPS mixture reacts from 90 °C, as indicated by the sudden loss of intensity of the reflections corresponding to the initial LZC and LPS phases and growth of LiCl reflections. For the LZC–LPSC system, the reflections corresponding to the initial LZC and LPSC phases become weaker and the LiCl peaks appear at ~280 °C. A better estimate of the onset temperature of the reaction between LZC and LPSC was obtained by conducting a sequential refinement of the *in situ* sXRD patterns using the LZC and LPSC structures as input. The R_{wp} parameter remains nearly unchanged up to 260 °C, as shown in Figure S2, but above that temperature the patterns could no longer be refined using only LZC and LPSC and the R_{wp} starts to increase due to the formation of degradation products. Hence, the onset temperature of the reaction between LZC and LPSC is assumed to be 260 °C hereafter.

2.1.2 Experimental strategy and analysis of solid electrolytes before mixing

Having established the onset reaction temperature of the two solid electrolyte pairings of interest, we heat treated a series of mixed LZC–LPS and LZC–LPSC pellets at various temperatures ranging from 25 °C to 300 °C. Our aim was two-fold: 1) to confirm the *in situ* heating synchrotron XRD results, and 2) to identify the reaction pathway for each mixture, leveraging the large contact area between the solid electrolyte powders to detect potential degradation products.

Each electrolyte was separately annealed at 300 °C for 12 hours before mixing to avoid any evolution caused by recrystallization of the individual phases during the heat treatment. XRD, ssNMR, and scanning electron microscopy (SEM) characterization of the annealed solid electrolytes can be found in Figures S3, S5, and S7, along with a description of the results. The diffraction results reveal a slight change in the polymorphic make-up of LZC,

together with a significant increase in crystallinity. In contrast, LPS becomes less crystalline and LPSC remains unchanged. The ssNMR results indicate relatively minor changes to the local structure of all solid electrolytes upon annealing. Interestingly, the ^{31}P ssNMR results reveal the presence of about 16.5 mol.% of γ-LPS ($Pmn2_1$) in the as-received LPS sample, which could not be resolved by XRD and is reduced to 5.2 mol.% upon annealing. The ^{6}Li ssNMR data obtained on the LZC samples indicate the presence of a LiCl impurity in the as-prepared sample that is presumably absorbed into the LZC phase upon annealing. The SEM images of the annealed powders suggest a distribution of particle sizes in all samples, with particles ranging from 30 nm to 2 µm for LZC, from 50 nm to 600 nm for LPS, and from 70 nm to 4 µm for LPSC. Windowless energy-dispersive X-ray spectroscopy (EDS) was also performed on the same samples to assess their oxygen (O) content, since O incorporation into a variety of solid electrolytes has been shown to affect their chemical and electrochemical stability.[67–69] While quantification is extremely difficult at the low accelerating voltages (here, 3 kV) required to probe light elements, such as O, the EDS results presented in Figures S4, S6, and S8 indicate only a very small amount of O in all of the samples. Oxygen is found to be homogeneously distributed in the LZC and LPSC samples, with only slight variations in O content across the LPS sample.

2.1.3 Monitoring chemical reactivity in the Li_2ZrCl_6–Li_3PS_4 system

LZC and LPS were mixed in a 1:1 molar ratio, and pellets were heat treated for 24 hours at either 25, 70, 110, 150, or 300 °C in vacuum-sealed quartz ampules. The heat-treated (HT-) samples are hereafter labeled according to their heat treatment temperature (e.g., HT-110 for a treatment at 110 °C).

XRD patterns obtained on the annealed LZC and LPS powders before mixing, as well as on the heat-treated mixed powder samples, are shown in Figure 2a. The patterns were obtained using a Kapton film to protect the samples from air exposure, yielding a strong

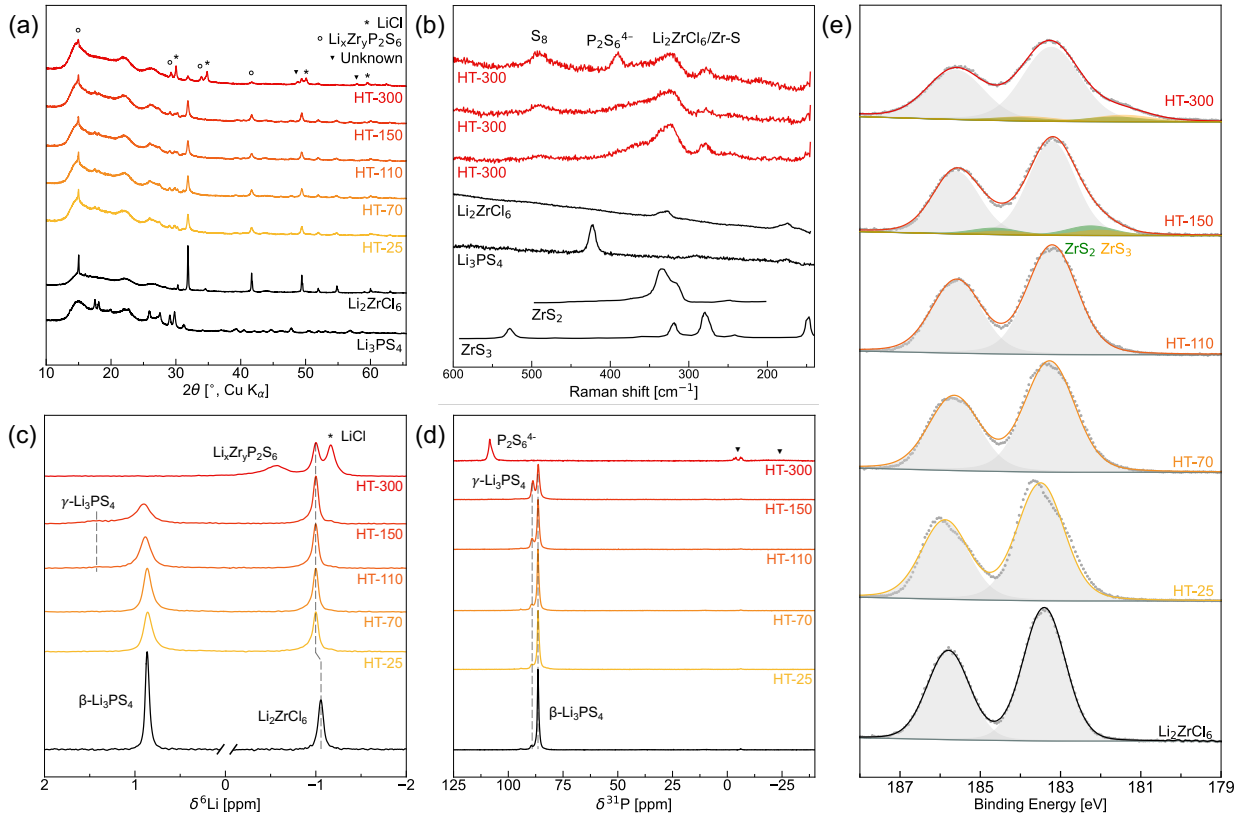

Figure 2: (a) XRD patterns obtained on annealed LZC and LPS samples, and on mixed pellets heat-treated for 24 hours at various temperatures (e.g., HT-110 stands for a heat treatment at 110 °C). Degradation phases observed in the HT-300 sample are marked with a ⋆ for LiCl, a ∘ for $Li_xZr_yP_2S_6$, and a ▼ when unassigned. (b) Raman spectra collected at various spots on the LZC–LPS HT-300 sample and on the annealed LZC and LPSC powders for reference. Spectra for ZrS_2 and ZrS_3 are digitized from previous reports: ZrS_2 data from Mañas-Valero et al.,[70] ZrS_3 data from Jin et al.[71] (c) Room temperature ^{6}Li and (d) ^{31}P ssNMR spectra obtained on the same series of samples at 18.8 T and 30 kHz MAS. The reference spectra in panel (c) were collected on annealed LPSC and annealed LZC before mixing and scaled to match the 1:1 molar ratio of the two compounds in the mixed powder samples. Unidentified degradation phases are indicated with a ▼. (e) Zr 3d XPS spectra obtained on annealed LZC and on the LZC–LPS mixed pellets.

background signal extending from 10° to 30° and making it difficult to observe some of the reflections from the LPS phase. The reflections in the HT-25 pattern are a superposition of the reflections observed in the individual LZC and LPS patterns, indicating that the

electrolyte mixture does not react at room temperature. The same reflections are also present in the HT-70 and HT-110 patterns. While the *in situ* heating sXRD data identified some reaction between the anolyte and catholyte from 90 °C, this could not be detected in the HT-110 sample likely due to the lower resolution of our lab XRD data and the intense Kapton background signal. The observed XRD reflections evolve to a small extent for the HT-150 sample and more extensively for the HT-300 sample. For example, the reflections attributed to LPS are no longer observed in the HT-300 pattern, indicating complete decomposition of this phase. In contrast, LZC only partially decomposes at 300 °C, as indicated by the decrease in the intensity of its main reflections at 15°, 32°, and 42°. Consistent with the *in situ* heating sXRD results, LiCl appears as a major decomposition phase, as indicated by the reflections marked with a ⋆ in Figure 2a. Still, LiCl alone does not account for all of the new reflections in the HT-300 pattern. We considered other binary compounds, such as Li_2S, ZrS_2, and ZrS_3, but none of these could explain the unassigned reflections (ZrS_2 could still be present as its diffraction peaks overlap with those of LZC). To facilitate the identification of more complex decomposition products, we turned to previous studies of the thermal[72] and electrochemical decomposition[73–75] of electrolytes containing PS_4^{3-} groups, such as LPS and LPSC. Those studies indicated the formation of phases comprising $P_2S_7^{4-}$ and $P_2S_6^{4-}$ units, hence, we considered the following ternary phases: $Li_4P_2S_6$,[76] Li_7PS_6,[77] ZrP_2S_6,[78] and ZrP_2S_7,[78] but to no avail. Instead, we found that some of the unassigned reflections matched those of the layered $Li_2MP_2S_6$ (M = V, Mn, Fe, Co, Ni, and Zn) thiophosphate phases reported by Sundaramoorthy et al.,[79,80] as shown in Figure S9a. Thus, we suspect that one of the unidentified phases is $Li_xZr_yP_2S_6$ with a layered structure similar to that depicted in Figure S9b. Its exact composition and structure cannot be ascertained due to the multiphasic and disordered nature of the HT-300 sample and poorly crystalline decomposition phases. These results motivate the use of local structure techniques to obtain additional information on the decomposition products.

Raman spectra obtained on annealed LPS and annealed LZC powders before mixing and at different locations on the surface of the HT-300 powder sample, are shown in Figure 2b. Only the HT-300 sample could be studied as the Raman spectra obtained on mixed samples heat treated to lower temperatures exhibited an intense fluorescence background due to LZC[40] (which, as discussed earlier, has partially decomposed by 300 °C), masking signals from other phases. The HT-300 Raman spectra show no sign of LPS remaining in the sample, in good agreement with the XRD results. The broad peak at 323 cm^{-1} matches the primary peak for LZC, but likely also comprises contributions from ZrS_2 and ZrS_3 decomposition phases.[70,71] The presence of ZrS_3 in the HT-300 sample is confirmed by the absorption bands at 150 cm^{-1} and 280 cm^{-1}, matching those observed for pure ZrS_3. The formation of $P_2S_6^{4-}$ dumbbells is evidenced by the absorption at 385 cm^{-1}.[81–83] The peak centered at 486 cm^{-1} and the weak signal at 220 cm^{-1} match the absorption bands expected for elemental sulfur, although a peak near 486 cm^{-1} is also observed for a pristine ampule (see Figure S10). Sulfur off-gassing at and above 150 °C is corroborated by the presence of a yellow residue at the surface of the HT-150 pellet and on the quartz tube used to prepare the HT-300 sample (see Figure S11).

Annealed LZC, annealed LPS, and heat-treated LZC–LPS samples were further investigated using ^6Li and ^{31}P ssNMR, with results shown in Figure 2c,d. The two resonances at 0.87 ppm and −1.05 ppm in the ^6Li spectra collected on annealed LPS and annealed LZC powders before mixing correspond to Li species in the LPS and LZC phases, respectively (Figure 2c). The reference ^{31}P spectrum collected on annealed LPS powder in Figure 2d comprises a major resonance at 86.5 ppm, attributed to β-LPS, and a minor resonance at 89.6 ppm ascribed to γ-LPS.[84] The ^6Li NMR spectra obtained on annealed LPS and LZC mixed together at room temperature (HT-25 sample), or heat treated to 70 °C (HT-70 sample), feature a slight downfield shift (higher ppm values) of the LZC resonance (Figure 2c) and an asymmetric broadening of the LZC and LPS resonances. This asymmetric broaden-

ing suggests Li chemical exchange between the LZC and LPS phases rather than reactivity. We determine an upper bound for the rate of Li exchange between LZC and LPS of 77 Hz, based on the (unmet) condition for signal coalescence ($k = \Omega_\Delta/(2\sqrt{2})$, where k is the rate of exchange and Ω_Δ is the separation of the two exchanging signals in Hz before mixing).[85] The stability of LZC and LPS up to 70 °C is confirmed by the very similar ^{31}P spectra obtained on annealed LPS and the HT-25 and HT-70 samples (Figure 2d). Noticeable changes to both the ^{6}Li and ^{31}P ssNMR spectra are observed upon heat treating a mixed pellet to 110 °C. The HT-110 ^{6}Li ssNMR spectrum exhibits a symmetrically broadened LPS resonance and a broad and low intensity signal at 1.37 ppm, which is ascribed to γ-LPS[86] and indicates partial decomposition of the β-LPS phase (Figure 2c). The formation of γ-LPS is corroborated by the growth of the ^{31}P resonance at 89.1 ppm (Figure 2d).[84] The HT-150 spectra reveal further growth of the γ-LPS phase at the expense of the initial β-LPS phase. Given that the LPS sample was annealed at 300 °C before mixing with LZC, the formation of γ-LPS in the HT-110 and HT-150 samples arises from chemical decomposition of β-LPS on contact with the LZC phase rather than a polymorphic transformation. The ssNMR results further confirm that the LPS phase has completely decomposed by 300 °C, while some LZC remains in the sample. The intense ^{6}Li ssNMR signal at −1.17 ppm reveals a large amount of LiCl in the sample, accounting for 32.5 % of the total Li content, in good agreement with the XRD results. The resonance at −1.00 ppm indicates residual LZC in the sample, accounting for an additional 31.9 % of the Li. The broad and asymmetric signal in the range of 100–115 ppm in the ^{31}P ssNMR spectrum can be fit with two components in a 2:1 ratio, which is consistent with the two P environments present in a 2:1 ratio in $P_2S_6^{4-}$ units, as found in $Li_4P_2S_6$.[81,87,88] However, the broad resonance at approximately −0.6 ppm in the ^{6}Li ssNMR spectrum is shifted upfield compared to the main ^{6}Li resonance reported for $Li_4P_2S_6$ compounds,[81,87,88] suggesting that the decomposition phase has a slightly different composition. We suggest that this is the layered $Li_xZr_yP_2S_6$ phase observed by XRD. This phase accounts

for the remaining 35.6 % of the Li in the HT-300 sample.

Zr 3d X-ray photoelectron (XPS) spectra collected on annealed LZC and on LZC–LPS mixed powder samples are presented in Figure 2e. The spectra collected on annealed LZC and on the mixed powders heat treated up to 110 °C comprise a single doublet attributed to the LZC phase with a Zr $3d_{5/2}$ binding energy of 183.4 eV.[38,40] Starting at 150 °C, spectral fits indicate the appearance of new doublets with Zr $3d_{5/2}$ peaks at 182.3 and 182.1 eV, attributed to ZrS_2[89,90] and ZrS_3,[89,91] respectively and in agreement with the Raman results. The ZrS_x peaks grow in intensity in the HT-300 spectrum, and a general broadening of all of the signals is observed, indicating decomposition of the LZC phase. Cl 2p, S 2p, and P 2p XPS spectra were also collected and are presented in Figure S12. These spectra provide further evidence for decomposition of the LZC–LPS sample at and above 150 °C.

Overall, the various techniques used in this work reveal that the LZC–LPS solid electrolyte combination does not react up to approximately 90 °C. The HT-300 sample comprises various decomposition phases, including LiCl, ZrS_2, ZrS_3, $Li_xZr_yP_2S_6$, and S_8, as well as residual LZC. A γ-LPS phase is formed at intermediate heat treatment temperatures of 110 and 150 °C.

2.1.4 Monitoring reactivity in the Li_2ZrCl_6–Li_6PS_5Cl system

XRD patterns obtained on the annealed LZC and LPSC powders before mixing, and on the heat-treated LZC–LPSC powder samples are presented in Figure 3a. No new peaks are observed in the patterns obtained on the mixed samples compared to the reference LZC and LPSC patterns up to at least 150 °C. In contrast, the reflections corresponding to the LPSC phase disappear in the HT-300 pattern, and we observe new reflections attributed to LiCl and to a layered $Li_xZr_yP_2S_6$ phase similar to that observed in the LZC–LPS HT-300 sample (Figure S9a). These new reflections are more intense than in the LZC–LPS HT-300 sample, which suggests that the reaction between LZC and LPSC forms a larger amount of LiCl

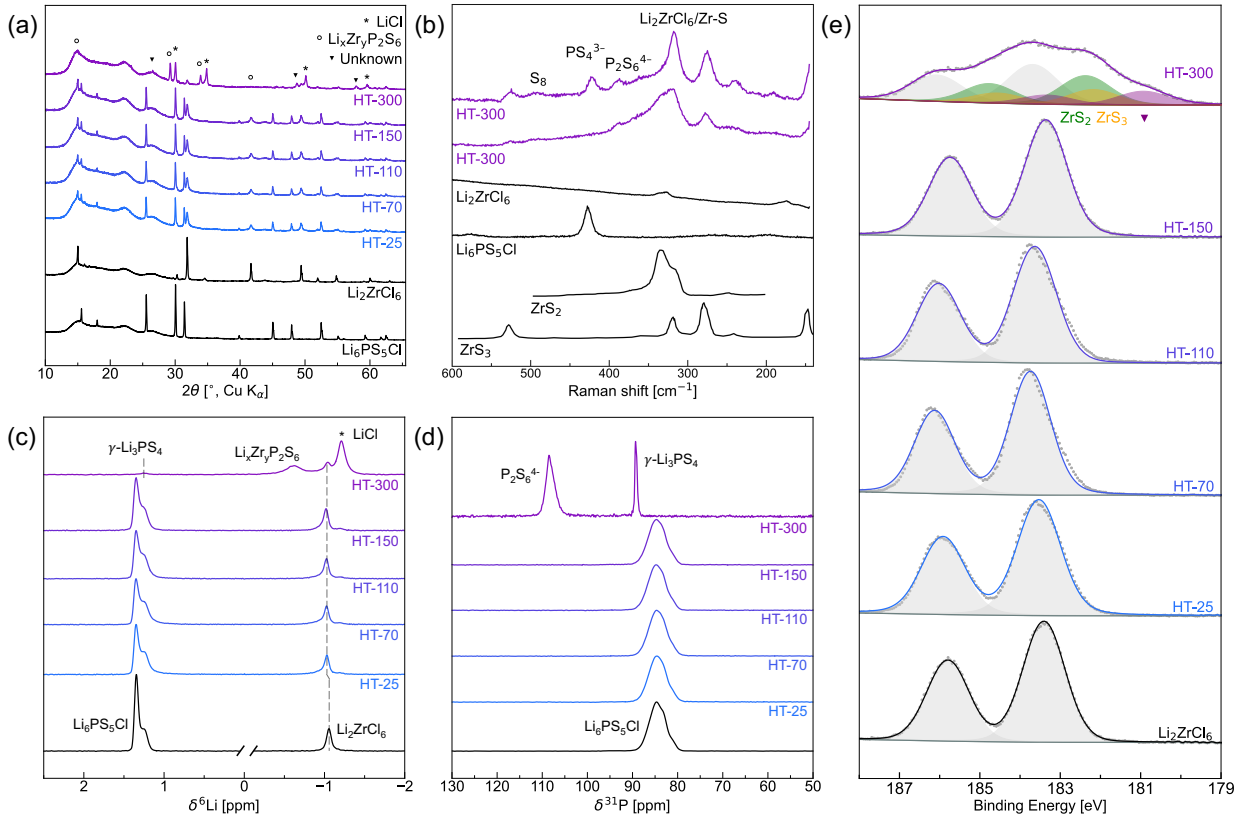

Figure 3: (a) XRD patterns obtained on annealed LZC and LPSC samples, and on mixed pellets heat-treated for 24 hours at various temperatures. Degradation phases observed in the HT-300 sample are marked with a ⋆ for LiCl, a ∘ for $Li_xZr_yP_2S_6$, and a ▼ when unassigned. (b) Raman spectra collected at various spots on the LZC–LPS HT-300 sample and on the annealed LZC and LPSC powders for reference. Spectra for ZrS_2 and ZrS_3 are digitized from previous reports: ZrS_2 data from Mañas-Valero et al.,[70] ZrS_3 data from Jin et al.[71] (c) ^{6}Li and (d) ^{31}P ssNMR spectra obtained on the same series of samples at 18.8 T and 30 kHz MAS. The reference spectra in panel (b) were collected on annealed LPSC and annealed LZC powders before mixing and scaled to match the 1:1 molar ratio of the two compounds present in the mixed powder samples. (e) Zr 3d XPS spectra obtained on annealed LZC and the LZC–LPSC mixed samples. The ▼ indicates an unassigned Zr environment, possibly $Li_xZr_yP_2S_6$.

and $Li_xZr_yP_2S_6$ degradation products. The LZC reflections become weaker in the HT-300 pattern, indicating partial decomposition of this phase.

The Raman spectra obtained on the annealed LZC and LPSC powders, and at different locations on the LZC–LPSC HT-300 sample, are presented in Figure 3b. Similar to the LZC–

LPS system, ZrS_2, ZrS_3, and $P_2S_6^{4-}$ moieties are detected in the HT-300 sample. The signal at 425 cm^{-1} is attributed to PS_4^{3-} units, potentially indicating the formation of LPS upon decomposition of LPSC. The quartz ampule used to prepare the HT-300 sample was also examined and the resulting Raman spectrum suggests the presence of ZrS_2 and $P_2S_6^{4-}$ moieties on the walls of the tube (see Figure S10). Finally, a weak signal is observed near 486 cm^{-1}, which, together with the appearance of a yellow hue on the HT-300 pellet and of yellow deposits on the walls of the quartz ampule (Figure S13), suggests that sulfur-containing gaseous species (likely including elemental sulfur) are evolved during decomposition.

^{6}Li and ^{31}P ssNMR spectra collected on the same set of LZC–LPSC samples are presented in Figure 3c,d (the ^{31}P ssNMR spectra are plotted over a wider frequency range in Figure S15). Similarly to the LZC–LPS system, upon mixing the LZC and LPSC powder samples at room temperature, the ^{6}Li resonance associated with each phase becomes asymmetrically broadened, indicating Li chemical exchange between the two electrolytes (here, an upper bound of 95 Hz is obtained for the rate of Li chemical exchange). Notably, the NMR results on the heat-treated powder mixtures confirm the remarkable stability of the LZC–LPSC pairing: the ^{6}Li and ^{31}P resonances remain largely unchanged and no new peaks appear up to at least 150 °C. However, after a 300 °C heat treatment, the ^{6}Li ssNMR spectrum comprises four signals. The weak signal at 1.25 ppm accounting for 2.3 % of the total ^{6}Li ssNMR signal intensity is attributed to γ-LPS; this assignment is corroborated by the presence of a γ-like PS_4^{3-} signal at 89.5 ppm in the ^{31}P spectrum[84,86] and is consistent with the Raman results presented earlier. The broad signal at ~ −0.6 ppm accounts for 32 % of the total ^{6}Li ssNMR signal intensity and is attributed to the layered $Li_xZr_yP_2S_6$ phase. The ^{31}P resonances arising from the two P environments present in the $P_2S_6^{4-}$ dumbbells of that phase are observed at ~108 ppm, as in the LZC–LPS system.[81,87,88] The ^{6}Li signal at −1.0 ppm, which accounts for 16 % of the signal intensity, indicates residual LZC in the sample. Finally, the LiCl signal at −1.2 ppm accounts for 50 % of the signal intensity. The

fraction of LZC remaining after the 300 °C heat treatment is lower when mixed with LPSC than with LPS (16 % vs. 32 %). From these results, we hypothesize that the reaction between LPSC and LZC is driven closer to completion after 24 hours, or consumes a higher molar fraction of LZC per mole of LPSC than per mole of LPS. The generation of more LiCl is in line with the higher Li and Cl content in Li_6PS_5Cl compared to Li_3PS_4.

Finally, the Zr 3*d* XPS spectra acquired on the annealed LZC and LPSC powders, and on the heat-treated LZC–LPSC samples, are presented in Figure 3e. The spectra obtained on the mixed samples heat-treated up to 150 °C show no degradation of the LZC phase. In contrast, the spectrum obtained on the HT-300 sample reveals the presence of ZrS_2 and ZrS_3, as well as a signal at lower binding energy (denoted by the ▼ in Figure 3e, with a $3d_{5/2}$ binding energy of ~180.9 eV) that may arise from the $Li_xZr_yP_2S_6$ phase or another unidentified phase. The Cl 2*p*, S 2*p*, and P 2*p* XPS spectra are shown in Figure S14 and described in detail in the Supplementary Information. These spectra show no evidence of decomposition up to 300 °C, where significant changes are observed in all of the spectra.

Overall, the LZC–LPSC solid electrolyte combination appears to be significantly more stable than the LZC–LPS pairing, with negligible degradation observed up to ~260 °C. Several decomposition phases detected after a 300 °C heat treatment are similar to those observed for the LZC–LPS system: LiCl, ZrS_2, ZrS_3, a layered $Li_xZr_yP_2S_6$ phase, and likely some amount of S_8. A γ-LPS phase is also observed in the HT-300 LZC–LPSC sample, which is only observed in the HT-110 and HT-150 samples in the case of LZC–LPS. We note that, while the average particle size of the annealed LPSC is larger than that of the annealed LPS, particle size effects are not significant. Indeed, additional stability tests were conducted on LZC–LPSC mixed pellets comprising smaller LPSC particles on average (average particle size of ~1 µm), with results presented in Figure S16. Despite the larger contact area between the LZC and LPSC particles, no degradation is observed at temperatures probed below 300 °C, and the relative fraction of decomposition phases observed by XRD and ssNMR in

the HT-300 sample is lower than when using larger LPSC particles.

2.2 Bilayer reactivity from first-principles calculations

Table 1: Reaction enthalpies ΔH (in kJ mol^{-1}) computed from first principles for the LZC–LPS and LZC–LPSC pairings.

LZC–LPS pairing	**ΔH**
$0.5714\,Li_3PS_4 + 0.4286\,Li_2ZrCl_6 \rightarrow 0.1429\,ZrP_2S_7 + 0.1429\,Zr(PS_3)_2 + 0.1429\,ZrS_3 + 2.571\,LiCl$	–59
$0.6667\,Li_3PS_4 + 0.3333\,Li_2ZrCl_6 \rightarrow 0.1667\,ZrP_2S_7 + 0.1667\,Li_4P_2S_6 + 0.1667\,ZrS_3 + 2\,LiCl$	–50
$0.7619\,Li_3PS_4 + 0.2381\,Li_2ZrCl_6 \rightarrow 0.2381\,ZrS_3 + 0.3333\,Li_4P_2S_6 + 0.04762\,P_2S_7 + 1.429\,LiCl$	–36
LZC–LPSC pairing	**ΔH**
$0.4444\,Li_6PS_5Cl + 0.5556\,Li_2ZrCl_6 \rightarrow 0.2222\,Zr(PS_3)_2 + 0.1111\,ZrS_2 + 0.2222\,ZrS_3 + 3.778\,LiCl$	–96
$0.5714\,Li_6PS_5Cl + 0.4286\,Li_2ZrCl_6 \rightarrow 0.1429\,ZrS_2 + 0.2857\,Li_4P_2S_6 + 0.2857\,ZrS_3 + 3.143\,LiCl$	–90
$0.6667\,Li_6PS_5Cl + 0.3333\,Li_2ZrCl_6 \rightarrow 0.3333\,ZrS_2 + 0.6667\,Li_3PS_4 + 2.6667\,LiCl$	–74

First-principles calculations were conducted to determine the thermodynamic driving force for decomposition of the LZC–LPS and LZC–LPSC pairings and identify possible reaction pathways. All binary, ternary, and quaternary phases (and relevant polymorphs) containing Li, Zr, P, S, and Cl in the Inorganic Crystal Structure Database (ICSD)[92] and the Materials Project database[93] were considered in this analysis. In addition, whenever the experimentally observed polymorph of LZC, LPS, or LPSC was found to be metastable (above the convex hull), its energy was lowered to bring it onto the hull. For example, although LPS forms various polymorphs,[94] the β-phase observed at ambient conditions was brought onto the hull. Additional calculation details can be found in Section S1.6. All chemical reactions derived from the Li-P-S-Cl-Zr phase diagram are listed in Table 1, along with their reaction enthalpies, ΔH. These reactions show negative ΔH values signifying a net driving force for chemical decomposition and confirming that neither LZC–LPS nor LZC–LPSC is thermodynamically stable. Given that the LZC, LPS, and LPSC electrolytes tested in this work likely present some amount of off-stoichiometry, e.g., due to Li and P volatility during synthesis,[95–97] favorable reactions identified based on a stoichiometric phase diagram may not be sufficient to accurately predict the decomposition products,[98] and combinations

of the reactions listed in Table 1 should be considered rather than the most favorable reaction (with the most negative ΔH). From this Table, the predicted decomposition products include binary phases such as ZrS_2, ZrS_3, LiCl, P_2S_7, and ternary phases such as ZrP_2S_7, $Zr(PS_3)_2$, and $Li_4P_2S_6$, all of which are thermodynamically stable. The formation of LiCl, ZrS_2, or ZrP_2S_7 results from metathesis with no oxidation state changes. In contrast, the formation of ZrS_3 or P_2S_7 involves partial oxidation of the S^{2-} anions in the initial Li_3PS_4 and Li_6PS_5Cl electrolytes to form discrete disulfide units, S_2^{2-}, or polysulfide chains, while the formation of $Zr(PS_3)_2$ and $Li_4P_2S_6$ results from reduction of P^{5+} in Li_3PS_4 and Li_6PS_5Cl to P^{4+}.

2.3 Relating the predicted and observed reactivity of chloride and thiophosphate solid electrolytes

The experimental and computational findings presented here provide complementary insights into the chemical compatibility of LZC with LPS or LPSC. The experimental results unequivocally show that the LZC–LPSC pairing is significantly more stable than LZC–LPS, with no sign of decomposition up to 260 °C on heating the combined powders (compared to 90 °C for LZC–LPS). By contrast, the reaction enthalpies predicted for the LZC–LPSC system, in the range of −74 to −90 kJ mol^{-1}, are greater than those predicted for the LZC–LPS system, ranging from −36 to −59 kJ mol^{-1}, suggesting more favorable decomposition of the former pairing. We believe that kinetic factors likely contribute to the observed stability of LZC–LPSC, which are not directly captured in our first-principles predictions. However, DFT calculations are the key to identifying possible decomposition products and thermodynamically stable solid electrolyte pairings, as shown in our recent work.[60]

Now, considering the reaction pathways of the two pairings, many of the computationally predicted decomposition phases are observed experimentally. Irrespective of the specific reaction pathway and pairing, LiCl is always predicted as a major decomposition product,

consistent with its significant and negative formation energy and in good agreement with its rapid formation from the onset of degradation of the electrolyte pair. Similarly, γ-Li_3PS_4 is predicted and observed on decomposition of LZC in contact with LPSC. For LZC–LPS, this phase is observed at intermediate heat treatment temperatures, consistent with the DFT results, indicating that it is not a stable degradation product. ZrS_x phases are predicted to form in all the reaction pathways listed in Table 1. They are also detected in the HT-300 sample for the two pairings, but the formation of *both* ZrS_2 and ZrS_3 is only correctly predicted for the LZC–LPSC system.

While the $Li_xZr_yP_2S_6$ observed in the HT-300 sample for the two pairings resembles the predicted $Li_4P_2S_6$ phase, its structure is more closely related to layered $Li_2MP_2S_6$ (M = V, Mn, Fe, Co, Ni, and Zn) compounds.[79] This prompted us to investigate the stability of two potential layered compounds, $LiZr(PS_3)_2$ and $Li_4Zr(PS_3)_4$, containing Zr^{3+} and Zr^{4+}, respectively. Although $LiZr(PS_3)_2$ was found to lie 70 meV/atom above the hull, $Li_4Zr(PS_3)_4$ was found to be metastable, lying only 26 meV/atom above the hull. Therefore, this compound is a possible decomposition product that is consistent with our experimental findings. Finally, the $Li_xZr_yP_2S_6$ phase appears to replace the predicted stable P_2S_7-containing phases predicted to form for the LZC–LPS pairing. This observation is in line with previous reports indicating that P_2S_7-containing phases can decompose into P_2S_6-containing phases and sulfur during a heat treatment.[83,87] A summary of possible sources of discrepancy between experimental observations and computational predictions of chemical compatibility is provided in Section S9 of the Supplementary Information.

2.4 Li-ion Transport in Bilayer LZC–LPSC Separators

The interface between the two solid electrolytes must both be stable and sufficiently conductive to Li-ions to enable high-performance dual-electrolyte solid-state batteries. In this section, we focus on the LZC–LPSC pairing and investigate Li^+-ion transport in the bulk of

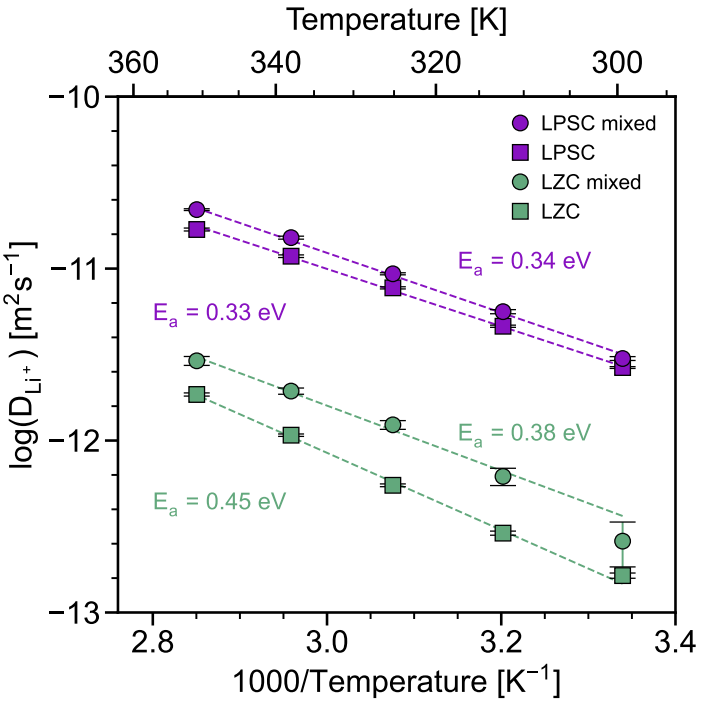

Figure 4: Li self-diffusion coefficients in the LZC and LPSC phases and corresponding activation energy barriers obtained from fits of the ^{7}Li PFG NMR data collected at 7.05 T on pressed pellets of as-synthesized LZC, as-received LPSC, and mixed LZC–LPSC.

the electrolytes and at their interface using microscopic and macroscopic methods.

^{7}Li pulsed-field gradient NMR (PFG-NMR) measurements were conducted on pellets of as-prepared LZC, as-received LPSC, and mixed LZC–LPSC (without any anneal or heat treatment) to monitor the evolution of the Li self-diffusion coefficients of the LZC and LPSC components upon mixing. The self-diffusion coefficient (D_{Li}) and activation energy barrier (E_{a}) for Li^{+}-ion transport within the LZC and LPSC phases before and after mixing and over the 26–78 °C range are plotted in Figure 4. Actual values and data acquisition parameters are listed in Tables S2 and S3, and a description of the PFG-NMR data analysis is provided in Section S10 of the Supplementary Information. A single Li diffusing environment is observed for each of the single-phase LPSC and LZC pellets: D_{Li} equals 2.66×10^{-12} and $1.64 \times 10^{-13}\,\mathrm{m^2\,s^{-1}}$, and E_{a} equals 0.33 eV and 0.44 eV for LPSC and LZC, respectively, at room temperature. These diffusivity values correspond to conductivities of $4.14\,\mathrm{mS\,cm^{-1}}$ for LPSC and $0.09\,\mathrm{mS\,cm^{-1}}$ for LZC, calculated using the Nernst-Einstein equation, which assumes uncorrelated Li^{+}-ion hops.[99,100] The diffusion length scale r probed in these experiments is determined using $r = \sqrt{6 D_{\mathrm{Li}} \Delta}$, where Δ is the diffusion time. r ranges from 1.1 to 2.3 µm for LPSC, and from 0.79 µm to 1.5 µm for LZC, over the 26–78 °C range (Table S2). Since LPSC particles are on the order of 70 nm to 4 µm, and LZC particles on the order of 30 nm to 2 µm (Figures S3c and S7d), the D_{Li} and E_{a} values reported represent a mixture of intra- and inter-grain diffusion.

Two Li diffusing environments are detected for the mixed LZC–LPSC pellet, which are attributed to the LPSC and LZC phases. The differing NMR relaxation properties (longitudinal or T_1, and transverse or T_2^*) of the two phases were leveraged to isolate the contribution from each to the overall ^{7}Li NMR signal decay and extract a phase-specific D_{Li} constant, as explained in more detail in Section S10. D_{Li} equals 3.00×10^{-12} and $2.60 \times 10^{-13}\,\mathrm{m^2\,s^{-1}}$, and E_{a} equals 0.34 eV and 0.38 eV, for LPSC and LZC, respectively, at room temperature. The LPSC-focused measurements probe diffusion lengths on the order of 1.2–1.3 µm, and

the LZC-focused experiments probe diffusion lengths on the order of 0.7–2.8 µm, and once again the D_{Li} and E_{a} values reported represent a mixture of intra- and inter-grain diffusion. Overall, for LPSC, D_{Li} and E_{a} increase slightly (within error for E_{a}) upon mixing. In contrast, for LZC, D_{Li} increases and E_{a} decreases significantly upon mixing. The apparent improvement in the Li^+-ion transport properties of the LZC component upon mixing is unlikely to result from improved transport within LZC grains and across their boundaries. It could instead be due to facile Li diffusion across or along the LZC–LPSC interface, and mixing in of Li^+-ion transport within the LPSC phase.

Further evidence for a Li-conductive LZC–LPSC interface comes from variable-temperature (VT) solid-state NMR measurements on a mixed LZC–LPSC powder sample (Figure S19). Here, the electrolytes were annealed separately to 300 °C before mixing to prevent any evolution of the NMR lineshape due to crystallization upon heating in the NMR probe, as has been observed in related systems.[30] Despite the reduced conductivity of the annealed LZC phase and measurement on a loose powder sample, the LZC and LPSC ^{6}Li resonances broaden and shift towards one another upon increasing the temperature from 34.7 to 67.8 °C, indicating slow Li chemical exchange between these two phases on the NMR timescale.[85]

To complement insights gained from NMR, electrochemical impedance spectroscopy (EIS) measurements were conducted at a series of temperatures from −70 to −48 °C on pressed pellets of as-milled LZC and as-received LPSC, and on LPSC|LZC|LPSC sandwich pellets. The parameters obtained from the fits and analysis of the EIS results are listed in Table S4. The procedure used to analyze the results is described in Section S12 in the Supplementary Information, along with a discussion of the results obtained on the single-phase pellets shown in Figures S20 and S21.

While the bulk and grain boundary contributions are successfully separated in the case of the single-layer pellets, significant overlap between the bulk and grain boundary contributions from the two electrolytes precludes a full deconvolution of the EIS spectra obtained on

the LPSC|LZC|LPSC sandwich pellet (Figure S22a), even when starting from the parameters derived from the single-phase pellets. However, the interfacial impedance contribution appears at sufficiently low frequencies[101] (higher time constants) that it can readily be separated from the bulk and grain boundary contributions using the distribution of relaxation times (DRT) method (Figure S22b). Fitting this contribution across the −70 to −48 °C temperature range yields capacitances varying from 1.1×10^{-7} to 7.3×10^{-6} F, i.e., in the range expected for conduction across an interface.[102] A room temperature interfacial resistance of 7 Ω (or 4.2 Ω cm^{-2}) is extrapolated from an Arrhenius fit of the low temperature data, along with an interfacial activation energy of 0.47 ± 0.02 eV (Figure S22c). The total impedance of the sandwich pellet was measured to be 453 Ω at room temperature, corresponding to a conductivity of 0.659 mS cm^{-1}. Thus, the interfacial resistance only accounts for 1.5 % of the pellet's total impedance, suggestive of facile Li^+ ion transport between the LZC and LPSC phases.

Finally, EIS measurements were conducted on the same LPSC|LZC|LPSC sandwich pellet after it was subjected to a 24-hour, 110 °C heat treatment under a uniaxial pressure of 75 MPa, with results presented in Figure S23. At room temperature, the total impedance of the pellet is 638 Ω and its conductivity is of 0.468 mS cm^{-1}. The increase in the pellet's impedance is primarily attributed to crystallization of LZC at moderate temperatures, which decreases its conductivity[55] as shown in Figure S24 and described in Section S12. The interfacial activation energy remains constant (within error from the fit) at 0.43±0.03 eV after the heat treatment. The room temperature interfacial resistance increases by an order of magnitude to 70 Ω (44 Ω cm^{-2}), but still only accounts for 11 % of the pellet's total impedance. Overall, the low interfacial resistances measured on the sandwich pellet underscore the formation of a highly conductive LZC–LPSC interface that is not drastically affected by a 110 °C heat treatment. Hence, this pairing is viable for dual-electrolyte solid-state batteries and compatible with typical processing and operating conditions.

2.5 Electrochemical performance of a dual electrolyte LZC-LPSC solid-state battery

Finally, the LZC–LPSC electrolyte pairing was tested in SSBs comprising a Li-In anode and a $LiNi_{0.8}Mn_{0.1}Co_{0.1}O_2$ (NMC811) + LZC + vapor-grown carbon fiber (VGCF) composite cathode. Duplicate cells were assembled using a $Li_{0.5}In$|LPSC|NMC811+LZC+VGCF single-layer or $Li_{0.5}In$|LPSC|LZC|NMC811+LZC+VGCF bilayer architecture and cycled at C/3 and 30 °C between 2.5–4.25 V vs. Li/Li^+ for 200 cycles for the single-layer cells and 500 cycles for the bilayer cells, after three formation cycles at C/10. The capacity retention of single-layer and bilayer cells over the first 200 cycles, averaged over duplicate cells, are plotted in Figure 5a, and representative voltage and differential capacity curves obtained during the second cycle at C/10 are presented in Figure 5b. The evolution of the electrochemical profile, discharge capacity and coulombic efficiency with cycling, for individual cells, is presented in Figures S25 and S26.

The bilayer cells show significantly higher capacity retention (90.0 % on average) than the single-layer cells (63.0 % on average) after 200 cycles, and an impressive 83.8 % capacity retention after 500 cycles, as shown in Figures S26a,b. Bilayer cells additionally exhibit a slightly lower voltage hysteresis, a higher energy density, and higher coulombic efficiencies on average than single-layer cells (see Table S5). While both cell architectures exhibit similar capacities and low overpotentials during the formation cycles (Figure 5b), the performance of the single-layer cells rapidly degrades, which is likely due to oxidation of the LPSC on contact with the NMC811 and VGCF components of the composite cathode during cycling. Hence, the additional layer of the LZC catholyte is necessary to maintain stable electrode-electrolyte interfaces and cycling performance. Although the capacity retention observed for both cell architectures is significantly higher than that reported for similar halide|thiophosphate dual electrolyte cells using polycrystalline transition metal oxide cathodes,[38,39,44,45,48,54,63] the spe-

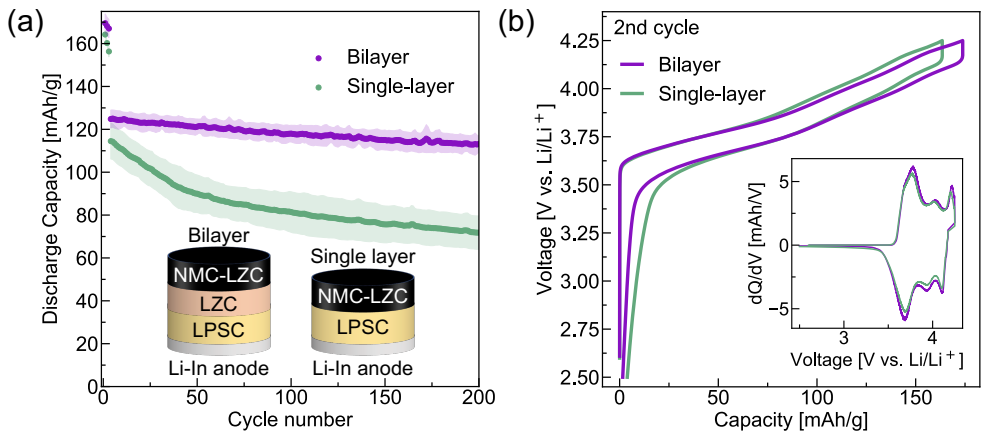

Figure 5: (a) Capacity retention of single-layer and bilayer LZC–LPSC cells cycled at C/3 and 30 °C between 4.25-2.5 V vs. Li/Li$^+$ after three formation cycles at C/10. The composite cathode comprises 66 wt.% NMC811, 31 wt.% LZC, and 3 wt.% VGCF, and the anode is $Li_{0.5}In$. Specific discharge capacities are computed with respect to the mass of active material in the composite cathode. Inset: Schematics of solid-state batteries with single-layer and bilayer architectures. (b) Representative electrochemical profiles obtained during the second cycle of galvanostatic cycling at C/10 for the single-layer and bilayer cell architectures. Inset: Corresponding differential capacity (dQ/dV) vs. voltage (V) curves.

cific capacities observed are still low relative to the theoretical capacity of the NMC811 cathode (200 mAh g^{-1}),[103] due in part to first-cycle irreversibilities (see Figure S27). Hence, further optimization of the synthesis and processing of component materials, of the electrode and cell architectures, and of cell assembly, is required to achieve greater cathode utilization, improve the cell's energy and power density, and further reduce the overpotential. For example, single-crystalline NMC811 and $LiNi_{0.88}Co_{0.11}Al_{0.01}O_2$(NCA88) cathodes have shown excellent capacity retention over 100-200 cycles in LZC–LPSC dual electrolyte cells,[37,55] and could be leveraged to further improve the cell performance demonstrated in this study.

Overall, the impressive capacity retention observed for bilayer LZC–LPSC cells indicates that this pairing is kinetically stabilized under normal battery operating conditions and could enable the development of high-energy-density solid-state batteries comprising a high-voltage oxide cathode and low-voltage metallic anode.

2.6 Design principles for stable electrified interfaces in electrochemical devices

Identifying component materials that form stable electrified interfaces is key to developing durable and performant electrochemical devices, including batteries, fuel cells, and sensors. In this section, we propose several criteria for designing such interfaces, drawing from the present study.

This work has revealed that an anolyte-catholyte pairing (LZC–LPSC) that is not thermodynamically stable may still form a kinetically stabilized interface over hundreds of charge-discharge cycles, showing promise for practical applications. We hereafter suggest possible factors contributing to the greater stability of the LZC–LPSC system compared to that of LZC–LPS. Since particle size effects were ruled out in an earlier section, we focus hereafter on compositional and structural factors. We first consider the impact of the oxidation state and size of the species present in the reacting phases on the kinetics of the decomposition process, and hypothesize that the higher the valence and the larger the size of the ion, the higher the energy barrier for ion migration, resulting in more sluggish decomposition reactions. Redox-type decomposition pathways will generally decrease the formal oxidation state of the species in the phases in contact, potentially increasing their propensity to migrate. For the two electrolyte pairings of interest, the migration of high-valent Zr^{4+} and P^{5+} species may be rate-limiting. In contrast, monovalent Li^{+} and Cl^{-} ions can readily migrate to form decomposition products. P^{5+} interdiffusion from PS_4^{3-} units also necessitates the breaking of four strong P-S bonds, which may further slow down the decomposition process. Given that the LZC–LPS and LZC–LPSC systems comprise similar species (albeit in different concentrations) and form similar decomposition products (with minor differences noted earlier), it is unlikely that the oxidation state and size of the ions in the starting and intermediate phases account for the apparent differences in decomposition kinetics. How-

ever, these parameters may be more generally relevant to materials selection when designing stable electrified interfaces.

Besides the oxidation state and size of the migrating species, the transformation pathway, including the distances over which high-valent species must migrate to form the decomposition product, likely influence the kinetics of the process. Using an opposite approach to topochemical reactions, where the crystal structure of the precursor dictates that of the product, we hypothesize that the more dissimilar the structures of the initial and decomposition phases, the slower the decomposition reaction. The shortest distance between P^{5+} species in LPS, LPSC, and in the proposed $Li_4Zr(PS_3)_4$ decomposition product are ~5.1, ~7.0, and ~2.3 Å, respectively. Hence, the apparent greater stability of the LZC–LPSC interface compared to LZC–LPS may result from P^{5+} species having to travel a significantly longer distance to form $P_2S_6^{4-}$ dumbbells starting from the argyrodite structure than from LPS. These observations suggest that structural disparity between the materials forming the interface and potential decomposition products is another relevant criterion for designing stable electrified interfaces.

The kinetics of LZC–LPSC degradation may be further impacted by the production of LiCl from the decomposition of both LPSC and LZC. According to Le Chatelier's principle, which states that if a chemical reaction is at equilibrium and experiences a change in the concentration of products or reactants, the equilibrium shifts in the opposite direction to offset the change, the formation of LiCl from decomposition of LZC or LPSC should impede further degradation, effectively stabilizing the interface. Hence, the design of stable electrified interfaces may benefit from using materials that share common decomposition products.

Rather than preventing or slowing down interfacial degradation, an alternative approach may be to harness the formation of passivating decomposition phases. To achieve this, the composition of the two materials in contact must be carefully optimized to favor the formation of decomposition products that are electronically insulating but conductive to the

ion of interest, preventing further degradation.

Overall, the results herein reveal a lack of fundamental understanding of reactivity at electrified interfaces. We propose several materials design principles toward developing stable interfaces, which we hope will be tested for various interfacial chemistries and applications.

3 Conclusion

In this study, the chemical and electrochemical compatibility between a chloride (Li_2ZrCl_6 (LZC)) and two common thiophosphate (Li_3PS_4 (LPS) and Li_6PS_5Cl (LPSC)) solid electrolyte materials were examined, in the search for a stable pairing for applications in energy-dense dual electrolyte solid-state batteries (SSBs). Chemical compatibility was assessed through heat treatments of solid electrolyte powder mixtures and a lower onset reaction temperature was determined for the Li_2ZrCl_6–Li_3PS_4 pairing (90 °C) compared to the Li_2ZrCl_6–Li_6PS_5Cl pairing (260 °C). The decomposition products were identified for each pairing using X-ray diffraction, solid-state nuclear magnetic resonance (ssNMR), X-ray photoelectron spectroscopy, and Raman spectroscopy. After a 300 °C heat treatment, the two pairings were found to form LiCl, a proposed layered $Li_xZr_yP_2S_6$ phase, ZrS_2 and ZrS_3, S_8, as well as γ–Li_3PS_4 for the LZC–LPSC pairing. Consistent with those findings, first-principles calculations indicated that neither pairing is thermodynamically stable. However, a higher reaction energy was predicted for the Li_2ZrCl_6–Li_6PS_5Cl combination, suggesting that sluggish reaction kinetics are responsible for its observed stability up to 260 °C. Focusing thereafter on the LZC–LPSC pairing, rapid Li-ion transport between the LZC and LPSC phases was evidenced by ssNMR, and a remarkably low interfacial resistance of $4.2\,\Omega\,cm^{-2}$ was determined by electrochemical impedance spectroscopy, accounting for only 1.5 % of the total resistance of a sandwich LPSC–LZC–LPSC pellet. The LZC–LPSC dual electrolyte was evaluated in SSBs comprising a $LiNi_{0.8}Mn_{0.1}Co_{0.1}O_2$ cathode and a Li-In anode. Although

dual electrolyte cells comprising a single electrolyte layer performed reasonably well, with 63.0 % of their initial capacity retained after 200 cycles, cells with a bilayer architecture exhibited a remarkable 90.0 % capacity retention under similar conditions, and 83.8 % capacity retention after 500 cycles. Those results indicate that the LZC–LPSC interface is kinetically stabilized under battery operating conditions, but an additional layer of the LZC catholyte between the LPSC electrolyte and the cathode composite is necessary to prevent any reactivity between the NMC811 cathode or conductive carbon and LPSC. Overall, we have identified a solid electrolyte pairing (LZC and LPSC) that is kinetically stabilized for hundreds of charge-discharge cycles and is highly conductive to Li-ions, showing great potential for use in energy-dense dual electrolyte SSBs. Based on these findings, we propose several criteria for designing stable electrified interfaces for a wide range of electrochemical devices.

Acknowledgement

This work was supported by LG Energy Solution through the UC San Diego Frontier Research Laboratory. E.S. and T.N.T.P. acknowledge support from the National Science Foundation Graduate Research Fellowship Program (NSF DGE 1650114 and 2139319). Any opinions, findings, and conclusions or recommendations expressed in this material are those of the author(s) and do not necessarily reflect the views of the National Science Foundation. P.C. acknowledges funding from the National Research Foundation under its NRF Fellowship NRFF12-2020-0012. The research reported here made use of the shared facilities of the Materials Research Science and Engineering Center (MRSEC) at UC Santa Barbara: NSF DMR-2308708. The UC Santa Barbara MRSEC is a member of the Materials Research Facilities Network (www.mrfn.com). Use was also made of the Laboratory for Surface Characterization Facility within the California NanoSystems Institute, supported by UC Santa

Barbara and the University of California, Office of the President. The computational work was performed using resources at the National Supercomputing Centre, Singapore (https://www.nscc.sg). The authors thank Dr. Ashley Cronk and Dr. So-Yeon Ham for their assistance with preliminary cell cycling and SEM, Dr. Amit Bhattacharya for assistance with the PFG-NMR measurements, Dr. Yu-Ting Chen for providing an LIC electrolyte sample, and Prof. Jeff Sakamoto for guidance with the EIS measurements.

Declaration of Interests

E.S., T.N.T.P., and R.J.C. have filed US and international patent applications based on this work. The remaining authors declare no competing interests.

Supporting Information Available

The Supporting Information is available free of charge at ···. Experimental Methods. Characterization of LIC–LPSC reactivity. Rietveld refinement of *in situ* synchrotron diffraction patterns obtained on mixed LZC–LPSC samples during heating. Characterization of LZC, LPS, and LPSC solid electrolytes. Identification of the $Li_xZr_yP_2S_6$ decomposition phase. Raman spectra of LZC–LPS and LZC–LPSC HT-300 ampules. Additional characterization of LZC–LPS mixed samples. Additional characterization of LZC–LPSC mixed samples. Possible sources of discrepancy between experimentally-observed and computationally-predicted chemical reactivity. Pulsed-field gradient NMR data acquisition and analysis. Variable temperature ^{6}Li solid-state NMR on LZC–LPSC mixed powder sample. Electrochemical impedance spectroscopy on LZC, LPSC, and LZC– LPSC pellets. Additional electrochemical testing results from dual-electrolyte LZC–LPSC solid-state batteries.

References

(1) Jung, K.-N.; Shin, H.-S.; Park, M.-S.; Lee, J.-W. Solid-State Lithium Batteries: Bipolar Design, Fabrication, and Electrochemistry. *ChemElectroChem* **2019**, *6*, 3842–3859.

(2) Janek, J.; Zeier, W. G. A Solid Future for Battery Development. *Nat Energy* **2016**, *1*, 1–4.

(3) Janek, J.; Zeier, W. G. Challenges in Speeding up Solid-State Battery Development. *Nat Energy* **2023**, *8*, 230–240.

(4) Banerjee, A.; Wang, X.; Fang, C.; Wu, E. A.; Meng, Y. S. Interfaces and Interphases in All-Solid-State Batteries with Inorganic Solid Electrolytes. *Chem. Rev.* **2020**, *120*, 6878–6933.

(5) Naik, K. G.; Vishnugopi, B. S.; Mukherjee, P. P. Heterogeneities Affect Solid-State Battery Cathode Dynamics. *Energy Storage Materials* **2023**, *55*, 312–321.

(6) Hu, J.; Young, R.; Lukic, B.; Broche, L.; Jervis, R.; Shearing, P.; Michiel, M.; Withers, P.; Rettie, A.; Paul, P. Quantifying Heterogeneous Degradation Pathways and Deformation Fields in Solid State Batteries. 2024.

(7) Kazyak, E.; Wang, M. J.; Lee, K.; Yadavalli, S.; Sanchez, A. J.; Thouless, M.; Sakamoto, J.; Dasgupta, N. P. Understanding the Electro-Chemo-Mechanics of Li Plating in Anode-Free Solid-State Batteries with Operando 3D Microscopy. *Matter* **2022**, *5*, 3912–3934.

(8) Tan, D. H. S.; Wu, E. A.; Nguyen, H.; Chen, Z.; Marple, M. A. T.; Doux, J.-M.; Wang, X.; Yang, H.; Banerjee, A.; Meng, Y. S. Elucidating Reversible Electrochemical Redox of Li6PS5Cl Solid Electrolyte. *ACS Energy Lett.* **2019**, *4*, 2418–2427.

(9) Patel, S. V.; Banerjee, S.; Liu, H.; Wang, P.; Chien, P.-H.; Feng, X.; Liu, J.; Ong, S. P.; Hu, Y.-Y. Tunable Lithium-Ion Transport in Mixed-Halide Argyrodites Li6–xPS5–xClBrx: An Unusual Compositional Space. *Chem. Mater.* **2021**, *33*, 1435–1443.

(10) Kato, Y.; Hori, S.; Saito, T.; Suzuki, K.; Hirayama, M.; Mitsui, A.; Yonemura, M.; Iba, H.; Kanno, R. High-Power All-Solid-State Batteries Using Sulfide Superionic Conductors. *Nat Energy* **2016**, *1*, 1–7.

(11) Kamaya, N.; Homma, K.; Yamakawa, Y.; Hirayama, M.; Kanno, R.; Yonemura, M.; Kamiyama, T.; Kato, Y.; Hama, S.; Kawamoto, K.; Mitsui, A. A Lithium Superionic Conductor. *Nature Mater* **2011**, *10*, 682–686.

(12) Golov, A.; Carrasco, J. Molecular-Level Insight into the Interfacial Reactivity and Ionic Conductivity of a Li-Argyrodite Li6PS5Cl Solid Electrolyte at Bare and Coated Li-Metal Anodes. *ACS Appl. Mater. Interfaces* **2021**, *13*, 43734–43745.

(13) Otto, S.-K.; Riegger, L. M.; Fuchs, T.; Kayser, S.; Schweitzer, P.; Burkhardt, S.; Henss, A.; Janek, J. In Situ Investigation of Lithium Metal–Solid Electrolyte Anode Interfaces with ToF-SIMS. *Advanced Materials Interfaces* **2022**, *9*, 2102387.

(14) Wenzel, S.; Sedlmaier, S. J.; Dietrich, C.; Zeier, W. G.; Janek, J. Interfacial Reactivity and Interphase Growth of Argyrodite Solid Electrolytes at Lithium Metal Electrodes. *Solid State Ionics* **2018**, *318*, 102–112.

(15) Kato, A.; Kowada, H.; Deguchi, M.; Hotehama, C.; Hayashi, A.; Tatsumisago, M. XPS and SEM Analysis between Li/Li3PS4 Interface with Au Thin Film for All-Solid-State Lithium Batteries. *Solid State Ionics* **2018**, *322*, 1–4.

(16) Li, Y.; Song, S.; Kim, H.; Nomoto, K.; Kim, H.; Sun, X.; Hori, S.; Suzuki, K.; Matsui, N.; Hirayama, M.; Mizoguchi, T.; Saito, T.; Kamiyama, T.; Kanno, R. A Lithium

Superionic Conductor for Millimeter-Thick Battery Electrode. *Science* **2023**, *381*, 50–53.

(17) Hayashi, A.; Masuzawa, N.; Yubuchi, S.; Tsuji, F.; Hotehama, C.; Sakuda, A.; Tatsumisago, M. A Sodium-Ion Sulfide Solid Electrolyte with Unprecedented Conductivity at Room Temperature. *Nat Commun* **2019**, *10*, 5266.

(18) Kerman, K.; Luntz, A.; Viswanathan, V.; Chiang, Y.-M.; Chen, Z. Review—Practical Challenges Hindering the Development of Solid State Li Ion Batteries. *J. Electrochem. Soc.* **2017**, *164*, A1731–A1744.

(19) Li, J.; Ma, C.; Chi, M.; Liang, C.; Dudney, N. J. Solid Electrolyte: The Key for High-Voltage Lithium Batteries. *Adv. Energy Mater.* **2015**, *5*, 1401408.

(20) Richards, W. D.; Miara, L. J.; Wang, Y.; Kim, J. C.; Ceder, G. Interface Stability in Solid-State Batteries. *Chem. Mater.* **2016**, *28*, 266–273.

(21) Tan, D. H. S. et al. Carbon-Free High-Loading Silicon Anodes Enabled by Sulfide Solid Electrolytes. *Science* **2021**, *373*, 1494–1499.

(22) Xiao, Y.; Wang, Y.; Bo, S.-H.; Kim, J. C.; Miara, L. J.; Ceder, G. Understanding Interface Stability in Solid-State Batteries. *Nat Rev Mater* **2020**, *5*, 105–126.

(23) Ren, Y. et al. Oxide-Based Solid-State Batteries: A Perspective on Composite Cathode Architecture. *Advanced Energy Materials* **2023**, *13*, 2201939.

(24) Wei, R.; Chen, S.; Gao, T.; Liu, W. Challenges, Fabrications and Horizons of Oxide Solid Electrolytes for Solid-State Lithium Batteries. *Nano Select* **2021**, *2*, 2256–2274.

(25) Deng, Z.; Mishra, T. P.; Mahayoni, E.; Ma, Q.; Tieu, A. J. K.; Guillon, O.; Chotard, J.-N.; Seznec, V.; Cheetham, A. K.; Masquelier, C.; Gautam, G. S.; Canepa, P. Fun-

damental Investigations on the Sodium-Ion Transport Properties of Mixed Polyanion Solid-State Battery Electrolytes. *Nat Commun* **2022**, *13*, 4470.

(26) Tieu, A. J. K.; Mahayoni, E.; Li, Y.; Deng, Z.; Fauth, F.; Chotard, J.-N.; Seznec, V.; Adams, S.; Masquelier, C.; Canepa, P. Zirconia-Free NaSICON Solid Electrolyte Materials for Sodium All-Solid-State Batteries. *J. Mater. Chem. A* **2023**, *11*, 23233–23242.

(27) Riegger, L. M.; Schlem, R.; Sann, J.; Zeier, W. G.; Janek, J. Lithium-Metal Anode Instability of the Superionic Halide Solid Electrolytes and the Implications for Solid-State Batteries. *Angew. Chem. Int. Ed.* **2021**, *60*, 6718–6723.

(28) Wang, S.; Bai, Q.; Nolan, A. M.; Liu, Y.; Gong, S.; Sun, Q.; Mo, Y. Lithium Chlorides and Bromides as Promising Solid-State Chemistries for Fast Ion Conductors with Good Electrochemical Stability. *Angew. Chem. Int. Ed.* **2019**, *58*, 8039–8043.

(29) Sebti, E.; Evans, H. A.; Chen, H.; Richardson, P. M.; White, K. M.; Giovine, R.; Koirala, K. P.; Xu, Y.; Gonzalez-Correa, E.; Wang, C.; Brown, C. M.; Cheetham, A. K.; Canepa, P.; Clément, R. J. Stacking Faults Assist Lithium-Ion Conduction in a Halide-Based Superionic Conductor. *J. Am. Chem. Soc.* **2022**, *144*, 5795–5811.

(30) Sebti, E.; Qi, J.; M. Richardson, P.; Ridley, P.; A. Wu, E.; Banerjee, S.; Giovine, R.; Cronk, A.; Ham, S.-Y.; Shirley Meng, Y.; Ping Ong, S.; J. Clément, R. Synthetic Control of Structure and Conduction Properties in Na–Y–Zr–Cl Solid Electrolytes. *Journal of Materials Chemistry A* **2022**, *10*, 21565–21578.

(31) Helm, B.; Schlem, R.; Wankmiller, B.; Banik, A.; Gautam, A.; Ruhl, J.; Li, C.; Hansen, M. R.; Zeier, W. G. Exploring Aliovalent Substitutions in the Lithium Halide Superionic Conductor Li3–xIn1–xZrxCl6 ($0 \leq x \leq 0.5$). *Chem. Mater.* **2021**, *33*, 4773–4782.

(32) Park, K.-H.; Kaup, K.; Assoud, A.; Zhang, Q.; Wu, X.; Nazar, L. F. High-Voltage Superionic Halide Solid Electrolytes for All-Solid-State Li-Ion Batteries. *ACS Energy Lett.* **2020**, *5*, 533–539.

(33) Li, X.; Liang, J.; Yang, X.; Adair, K. R.; Wang, C.; Zhao, F.; Sun, X. Progress and Perspectives on Halide Lithium Conductors for All-Solid-State Lithium Batteries. *Energy Environ. Sci.* **2020**, *13*, 1429–1461.

(34) Liang, J.; Li, X.; Wang, S.; Adair, K. R.; Li, W.; Zhao, Y.; Wang, C.; Hu, Y.; Zhang, L.; Zhao, S.; Lu, S.; Huang, H.; Li, R.; Mo, Y.; Sun, X. Site-Occupation-Tuned Superionic Li_xScCl_{3+x} Halide Solid Electrolytes for All-Solid-State Batteries. *J. Am. Chem. Soc.* **2020**, *142*, 7012–7022.

(35) Park, J.; Han, D.; Kwak, H.; Han, Y.; Choi, Y. J.; Nam, K.-W.; Jung, Y. S. Heat Treatment Protocol for Modulating Ionic Conductivity via Structural Evolution of $Li_{3-x}Yb_{1-x}M_xCl_6$ (M = Hf^{4+}, Zr^{4+}) New Halide Superionic Conductors for All-Solid-State Batteries. *Chem. Eng. J.* **2021**, *425*, 130630.

(36) Kim, S. Y.; Kaup, K.; Park, K.-H.; Assoud, A.; Zhou, L.; Liu, J.; Wu, X.; Nazar, L. F. Lithium Ytterbium-Based Halide Solid Electrolytes for High Voltage All-Solid-State Batteries. *ACS Mater. Lett.* **2021**, 930–938.

(37) Kwak, H.; Han, D.; Lyoo, J.; Park, J.; Jung, S. H.; Han, Y.; Kwon, G.; Kim, H.; Hong, S.-T.; Nam, K.-W.; Jung, Y. S. New Cost-Effective Halide Solid Electrolytes for All-Solid-State Batteries: Mechanochemically Prepared Fe3+-Substituted Li2ZrCl6. *Advanced Energy Materials* **2021**, *11*, 2003190.

(38) Luo, X.; Zhong, Y.; Wang, X.; Xia, X.; Gu, C.; Tu, J. Ionic Conductivity Enhancement of Li2ZrCl6 Halide Electrolytes via Mechanochemical Synthesis for All-Solid-State Lithium–Metal Batteries. *ACS Appl. Mater. Interfaces* **2022**, *14*, 49839–49846.

(39) Chen, S.; Yu, C.; Chen, S.; Peng, L.; Liao, C.; Wei, C.; Wu, Z.; Cheng, S.; Xie, J. Enabling Ultrafast Lithium-Ion Conductivity of Li2ZrCl6 by Indium Doping. *Chinese Chemical Letters* **2022**, *33*, 4635–4639.

(40) Cronk, A.; Chen, Y.-T.; Deysher, G.; Ham, S.-Y.; Yang, H.; Ridley, P.; Sayahpour, B.; Nguyen, L. H. B.; Oh, J. A. S.; Jang, J.; Tan, D. H. S.; Meng, Y. S. Overcoming the Interfacial Challenges of LiFePO4 in Inorganic All-Solid-State Batteries. *ACS Energy Lett.* **2023**, *8*, 827–835.

(41) Wu, E. A. et al. A Stable Cathode-Solid Electrolyte Composite for High-Voltage, Long-Cycle-Life Solid-State Sodium-Ion Batteries. *Nat Commun* **2021**, *12*, 1256.

(42) Koç, T.; Marchini, F.; Rousse, G.; Dugas, R.; Tarascon, J.-M. In Search of the Best Solid Electrolyte-Layered Oxide Pairing for Assembling Practical All-Solid-State Batteries. *ACS Appl. Energy Mater.* **2021**, *4*, 13575–13585.

(43) Kim, J. S.; Jung, S.; Kwak, H.; Han, Y.; Kim, S.; Lim, J.; Lee, Y. M.; Jung, Y. S. Synergistic Halide-Sulfide Hybrid Solid Electrolytes for Ni-rich Cathodes Design Guided by Digital Twin for All-Solid-State Li Batteries. *Energy Storage Materials* **2023**, *55*, 193–204.

(44) Rosenbach, C.; Walther, F.; Ruhl, J.; Hartmann, M.; Hendriks, T. A.; Ohno, S.; Janek, J.; Zeier, W. G. Visualizing the Chemical Incompatibility of Halide and Sulfide-Based Electrolytes in Solid-State Batteries. *Advanced Energy Materials* **2023**, *13*, 2203673.

(45) Tron, A.; Beutl, A.; Mohammad, I.; Paolella, A. Insights into the Chemical and Electrochemical Behavior of Halide and Sulfide Electrolytes in All-Solid-State Batteries. *Energy Adv.* **2025**,

(46) Ye, Q.; Li, X.; Zhang, W.; Xia, Y.; He, X.; Huang, H.; Gan, Y.; Xia, X.; Zhang, J. Slurry-Coated LiNi0.8Co0.1Mn0.1O2–Li3InCl6 Composite Cathode with Enhanced Interfacial Stability for Sulfide-Based All-Solid-State Batteries. *ACS Appl. Mater. Interfaces* **2023**, *15*, 18878–18888.

(47) Kwak, H.; Kim, J.-S.; Han, D.; Kim, J. S.; Park, J.; Kwon, G.; Bak, S.-M.; Heo, U.; Park, C.; Lee, H.-W.; Nam, K.-W.; Seo, D.-H.; Jung, Y. S. Boosting the Interfacial Superionic Conduction of Halide Solid Electrolytes for All-Solid-State Batteries. *Nat Commun* **2023**, *14*, 2459.

(48) Wang, C.; Liang, J.; Luo, J.; Liu, J.; Li, X.; Zhao, F.; Li, R.; Huang, H.; Zhao, S.; Zhang, L.; Wang, J.; Sun, X. A Universal Wet-Chemistry Synthesis of Solid-State Halide Electrolytes for All-Solid-State Lithium-Metal Batteries. *Sci. Adv.* **2021**, *7*, eabh1896.

(49) Wang, H.; Li, Y.; Tang, Y.; Ye, D.; He, T.; Zhao, H.; Zhang, J. Electrochemically Stable Li3–xIn1–xHfxCl6 Halide Solid Electrolytes for All-Solid-State Batteries. *ACS Appl. Mater. Interfaces* **2023**, *15*, 5504–5511.

(50) Deng, Z.; Jin, Z.; Chen, D.; Ni, D.; Tian, M.; Zhan, Y.; Li, S.; Sun, Y.; Huang, X.; Zhao, Y. Bilayer Halide Electrolytes for All-Inorganic Solid-State Lithium-Metal Batteries with Excellent Interfacial Compatibility. *ACS Appl. Mater. Interfaces* **2022**, *14*, 48619–48626.

(51) Li, X.; Liang, J.; Chen, N.; Luo, J.; Adair, K. R.; Wang, C.; Banis, M. N.; Sham, T.-K.; Zhang, L.; Zhao, S.; Lu, S.; Huang, H.; Li, R.; Sun, X. Water-Mediated Synthesis of a Superionic Halide Solid Electrolyte. *Angewandte Chemie International Edition* **2019**, *58*, 16427–16432.

(52) Hendriks, T. A.; Lange, M. A.; Kiens, E. M.; Baeumer, C.; Zeier, W. G. Balancing Partial Ionic and Electronic Transport for Optimized Cathode Utilization of High-Voltage $LiMn_2O_4$/Li_3InCl_6 Solid-State Batteries. *Batteries & Supercaps* **2023**, *6*, e202200544.

(53) Ji, W.; Zheng, D.; Zhang, X.; Ding, T.; Qu, D. A Kinetically Stable Anode Interface for Li3YCl6-based All-Solid-State Lithium Batteries. *J. Mater. Chem. A* **2021**, *9*, 15012–15018.

(54) Zhang, H.; Yu, Z.; Cheng, J.; Chen, H.; Huang, X.; Tian, B. Halide/Sulfide Composite Solid-State Electrolyte for Li-anode Based All-Solid-State Batteries. *Chinese Chemical Letters* **2023**, *34*, 108228.

(55) Wang, K.; Ren, Q.; Gu, Z.; Duan, C.; Wang, J.; Zhu, F.; Fu, Y.; Hao, J.; Zhu, J.; He, L.; Wang, C.-W.; Lu, Y.; Ma, J.; Ma, C. A Cost-Effective and Humidity-Tolerant Chloride Solid Electrolyte for Lithium Batteries. *Nat Commun* **2021**, *12*, 4410.

(56) Luo, X.; Cai, D.; Wang, X.; Xia, X.; Gu, C.; Tu, J. A Novel Ethanol-Mediated Synthesis of Superionic Halide Electrolytes for High-Voltage All-Solid-State Lithium–Metal Batteries. *ACS Appl. Mater. Interfaces* **2022**, *14*, 29844–29855.

(57) Koç, T.; Hallot, M.; Quemin, E.; Hennequart, B.; Dugas, R.; Abakumov, A. M.; Lethien, C.; Tarascon, J.-M. Toward Optimization of the Chemical/Electrochemical Compatibility of Halide Solid Electrolytes in All-Solid-State Batteries. *ACS Energy Lett.* **2022**, *7*, 2979–2987.

(58) Zhou, L.; Kwok, C. Y.; Shyamsunder, A.; Zhang, Q.; Wu, X.; Nazar, L. F. A New Halospinel Superionic Conductor for High-Voltage All Solid State Lithium Batteries. *Energy Environ. Sci.* **2020**, *13*, 2056–2063.

(59) Samanta, S.; Bera, S.; Biswas, R. K.; Mondal, S.; Mandal, L.; Banerjee, A. Ionocovalency of the Central Metal Halide Bond-Dependent Chemical Compatibility of Halide Solid Electrolytes with Li $_6$ PS $_5$ Cl. *ACS Energy Lett.* **2024**, 3683–3693.

(60) Panchal, A. A.; Pennebaker, T. N.; Sebti, E.; Li, Y.; Li, Y.; Clément, R. J.; Canepa, P. Compatibility of Halide Bilayer Separators for All-Solid-State Batteries. *ACS Energy Lett.* **2024**, 5935–5944.

(61) Song, Z. et al. Promoting High-Voltage Stability through Local Lattice Distortion of Halide Solid Electrolytes. *Nat Commun* **2024**, *15*, 1481.

(62) Kim, Y.; Juarez-Yescas, C.; Liao, D. W.; Jangid, M. K.; Joshi, P.; Yang, H.; Zahiri, B.; Braun, P. V.; Dasgupta, N. P. Thin Free-Standing Sulfide/Halide Bilayer Electrolytes for Solid-State Batteries Using Slurry Processing and Lamination. *ACS Energy Lett.* **2024**, *9*, 1353–1360.

(63) Kochetkov, I.; Zuo, T.-T.; Ruess, R.; Singh, B.; Zhou, L.; Kaup, K.; Janek, J.; Nazar, L. Different Interfacial Reactivity of Lithium Metal Chloride Electrolytes with High Voltage Cathodes Determines Solid-State Battery Performance. *Energy Environ. Sci.* **2022**, 10.1039.D2EE00803C.

(64) Zhou, L.; Zuo, T.-T.; Kwok, C. Y.; Kim, S. Y.; Assoud, A.; Zhang, Q.; Janek, J.; Nazar, L. F. High Areal Capacity, Long Cycle Life 4 V Ceramic All-Solid-State Li-ion Batteries Enabled by Chloride Solid Electrolytes. *Nat Energy* **2022**, *7*, 83–93.

(65) Emsley, J. The A–Z of Zirconium. *Nature Chem* **2014**, *6*, 254–254.

(66) Boulineau, S.; Courty, M.; Tarascon, J.-M.; Viallet, V. Mechanochemical Synthesis of Li-argyrodite Li6PS5X (X=Cl, Br, I) as Sulfur-Based Solid Electrolytes for All Solid State Batteries Application. *Solid State Ionics* **2012**, *221*, 1–5.

(67) Indrawan, R. F.; Matsuda, R.; Hikima, K.; Matsuda, A. Enhanced Electrochemistry Stability of Oxygen Doped Li6PS5Cl Argyrodite Solid Electrolyte by Liquid-Phase Synthesis. *Solid State Ionics* **2023**, *401*, 116344.

(68) Sun, Y.; Suzuki, K.; Hara, K.; Hori, S.; Yano, T.-a.; Hara, M.; Hirayama, M.; Kanno, R. Oxygen Substitution Effects in Li10GeP2S12 Solid Electrolyte. *Journal of Power Sources* **2016**, *324*, 798–803.

(69) Cao, K.; Xia, Y.; Li, H.; Huang, H.; Iqbal, S.; Yousaf, M.; Bin Xu, B.; Sun, W.; Yan, M.; Pan, H.; Jiang, Y. Oxygen-Regulated Spontaneous Solid Electrolyte Interphase Enabling Ultra-Stable Solid-State Na Metal Batteries. *Science Bulletin* **2024**, *69*, 49–58.

(70) Mañas-Valero, S.; García-López, V.; Cantarero, A.; Galbiati, M. Raman Spectra of ZrS2 and ZrSe2 from Bulk to Atomically Thin Layers. *Applied Sciences* **2016**, *6*, 264.

(71) Jin, H.; Cheng, D.; Li, J.; Cao, X.; Li, B.; Wang, X.; Liu, X.; Zhao, X. Facile Synthesis of Zirconium Trisulfide and Hafnium Trisulfide Nanobelts: Growth Mechanism and Raman Spectroscopy. *Solid State Sciences* **2011**, *13*, 1166–1171.

(72) Aoki, Y.; Ogawa, K.; Nakagawa, T.; Hasegawa, Y.; Sakiyama, Y.; Kojima, T.; Tabuchi, M. Chemical and Structural Changes of 70Li2S-30P2S5 Solid Electrolyte during Heat Treatment. *Solid State Ionics* **2017**, *310*, 50–55.

(73) Ohno, S.; Rosenbach, C.; Dewald, G. F.; Janek, J.; Zeier, W. G. Linking Solid Electrolyte Degradation to Charge Carrier Transport in the Thiophosphate-Based Composite Cathode toward Solid-State Lithium-Sulfur Batteries. *Advanced Functional Materials* **2021**, *31*, 2010620.

(74) Koerver, R.; Walther, F.; Aygün, I.; Sann, J.; Dietrich, C.; Zeier, W. G.; Janek, J.

Redox-Active Cathode Interphases in Solid-State Batteries. *J. Mater. Chem. A* **2017**, *5*, 22750–22760.

(75) Dietrich, C.; Koerver, R.; Gaultois, M. W.; Kieslich, G.; Cibin, G.; Janek, J.; Zeier, W. G. Spectroscopic Characterization of Lithium Thiophosphates by XPS and XAS – a Model to Help Monitor Interfacial Reactions in All-Solid-State Batteries. *Phys. Chem. Chem. Phys.* **2018**, *20*, 20088–20095.

(76) Hood, Z. D.; Kates, C.; Kirkham, M.; Adhikari, S.; Liang, C.; Holzwarth, N. A. W. Structural and Electrolyte Properties of Li4P2S6. *Solid State Ionics* **2016**, *284*, 61–70.

(77) Kong, S. T.; Gün, Ö.; Koch, B.; Deiseroth, H. J.; Eckert, H.; Reiner, C. Structural Characterisation of the Li Argyrodites Li7PS6 and Li7PSe6 and Their Solid Solutions: Quantification of Site Preferences by MAS-NMR Spectroscopy. *Chemistry – A European Journal* **2010**, *16*, 5138–5147.

(78) Lott, D. R.; Fincher, T.; LeBret, G. C.; Cleary, D. A.; Breneman, G. L. Synthesis and Crystal Structure of ZrP2S6and ZrP2S7. *Journal of Solid State Chemistry* **1999**, *143*, 239–245.

(79) Sundaramoorthy, S.; Gerasimchuk, N.; Ghosh, K.; Kelley, S. P.; Choudhury, A. Li2MP2S6: Building-Block Approach to a Family of 2D Non-van Der Waals-Layered Materials and Their Water, Ammonia, and Ion Intercalation Properties. *Chem. Mater.* **2024**, *36*, 3574–3587.

(80) Iton, Z. W. B.; Irving-Singh, Z.; Hwang, S.-J.; Bhattacharya, A.; Shaker, S.; Das, T.; Clément, R. J.; Goddard, W. A. I.; See, K. A. Modular MPS3-Based Frameworks for Superionic Conduction of Monovalent and Multivalent Ions. *J. Am. Chem. Soc.* **2024**, *146*, 24398–24414.

(81) Dietrich, C.; Weber, D. A.; Culver, S.; Senyshyn, A.; Sedlmaier, S. J.; Indris, S.; Janek, J.; Zeier, W. G. Synthesis, Structural Characterization, and Lithium Ion Conductivity of the Lithium Thiophosphate Li2P2S6. *Inorg. Chem.* **2017**, *56*, 6681–6687.

(82) Preefer, M. B.; Grebenkemper, J. H.; Schroeder, F.; Bocarsly, J. D.; Pilar, K.; Cooley, J. A.; Zhang, W.; Hu, J.; Misra, S.; Seeler, F.; Schierle-Arndt, K.; Seshadri, R. Rapid and Tunable Assisted-Microwave Preparation of Glass and Glass-Ceramic Thiophosphate "Li7P3S11" Li-Ion Conductors. *ACS Appl. Mater. Interfaces* **2019**, *11*, 42280–42287.

(83) Mercier, R.; Malugani, J. P.; Fahys, B.; Douglande, J.; Robert, G. Synthese, Structure Cristalline et Analyse Vibrationnelle de l'hexathiohypodiphosphate de Lithium Li4P2S6. *Journal of Solid State Chemistry* **1982**, *43*, 151–162.

(84) Kudu, Ö. U.; Famprikis, T.; Cretu, S.; Porcheron, B.; Salager, E.; Demortiere, A.; Courty, M.; Viallet, V.; Mercier, T. L.; Fleutot, B.; Braida, M.-D.; Masquelier, C. Structural Details in Li3PS4: Variety in Thiophosphate Building Blocks and Correlation to Ion Transport. *Energy Storage Materials* **2022**, *44*, 168–179.

(85) Levitt, M. H. *Spin Dynamics Basics of Nuclear Magnetic Resonance*, 2nd ed.; John Wiley & Sons, Ltd, 2008.

(86) Gobet, M.; Greenbaum, S.; Sahu, G.; Liang, C. Structural Evolution and Li Dynamics in Nanophase Li3PS4 by Solid-State and Pulsed-Field Gradient NMR. *Chem. Mater.* **2014**, *26*, 3558–3564.

(87) Eckert, H.; Zhang, Z.; Kennedy, J. H. Structural Transformation of Non-Oxide Chalcogenide Glasses. The Short-Range Order of Lithium Sulfide (Li2S)-Phosphorus Pentasulfide (P2S5) Glasses Studied by Quantitative Phosphorus-31, Lithium-6, and Lithium-7 High-Resolution Solid-State NMR. *Chem. Mater.* **1990**, *2*, 273–279.

(88) Neuberger, S.; Culver, S. P.; Eckert, H.; Zeier, W. G.; auf der Günne, J. S. Refinement of the Crystal Structure of Li4P2S6 Using NMR Crystallography. *Dalton Trans.* **2018**, *47*, 11691–11695.

(89) Jellinek, F.; Pollak, R. A.; Shafer, M. W. X-Ray Photoelectron Spectra and Electronic Structure of Zirconium Trisulfide and Triselenide. *Materials Research Bulletin* **1974**, *9*, 845–856.

(90) Jin, Y.; Sun, J.; Zhang, L.; Yang, J.; Wu, Y.; You, B.; Liu, X.; Leng, K.; Liu, S. Controllable Oxidation of ZrS2 to Prepare High-κ, Single-Crystal m-ZrO2 for 2D Electronics. *Advanced Materials* **2023**, *35*, 2212079.

(91) Zakharova, O. V.; Gusev, A. A.; Abourahma, J.; Vorobeva, N. S.; Sokolov, D. V.; Muratov, D. S.; Kuznetsov, D. V.; Sinitskii, A. Nanotoxicity of ZrS3 Probed in a Bioluminescence Test on E. Coli Bacteria: The Effect of Evolving H2S. *Nanomaterials* **2020**, *10*, 1401.

(92) Belsky, A.; Hellenbrandt, M.; Karen, V. L.; Luksch, P. New Developments in the Inorganic Crystal Structure Database (ICSD): Accessibility in Support of Materials Research and Design. *Acta Crystallogr B Struct Sci* **2002**, *58*, 364–369.

(93) Jain, A.; Ong, S. P.; Hautier, G.; Chen, W.; Richards, W. D.; Dacek, S.; Cholia, S.; Gunter, D.; Skinner, D.; Ceder, G.; Persson, K. A. Commentary: The Materials Project: A Materials Genome Approach to Accelerating Materials Innovation. *APL Materials* **2013**, *1*, 011002.

(94) Homma, K.; Yonemura, M.; Kobayashi, T.; Nagao, M.; Hirayama, M.; Kanno, R. Crystal Structure and Phase Transitions of the Lithium Ionic Conductor Li3PS4. *Solid State Ionics* **2011**, *182*, 53–58.

(95) Kraft, M. A.; Culver, S. P.; Calderon, M.; Böcher, F.; Krauskopf, T.; Senyshyn, A.; Dietrich, C.; Zevalkink, A.; Janek, J.; Zeier, W. G. Influence of Lattice Polarizability on the Ionic Conductivity in the Lithium Superionic Argyrodites Li6PS5X (X = Cl, Br, I). *J. Am. Chem. Soc.* **2017**, *139*, 10909–10918.

(96) Gautam, A.; Sadowski, M.; Prinz, N.; Eickhoff, H.; Minafra, N.; Ghidiu, M.; Culver, S. P.; Albe, K.; Fässler, T. F.; Zobel, M.; Zeier, W. G. Rapid Crystallization and Kinetic Freezing of Site-Disorder in the Lithium Superionic Argyrodite Li6PS5Br. *Chem. Mater.* **2019**, *31*, 10178–10185.

(97) Minafra, N.; Kraft, M. A.; Bernges, T.; Li, C.; Schlem, R.; Morgan, B. J.; Zeier, W. G. Local Charge Inhomogeneity and Lithium Distribution in the Superionic Argyrodites Li6PS5X (X = Cl, Br, I). *Inorg. Chem.* **2020**, *59*, 11009–11019.

(98) Gorai, P.; Famprikis, T.; Singh, B.; Stevanović, V.; Canepa, P. Devil Is in the Defects: Electronic Conductivity in Solid Electrolytes. *Chem. Mater.* **2021**, *33*, 7484–7498.

(99) Baktash, A.; Reid, J. C.; Roman, T.; Searles, D. J. Diffusion of Lithium Ions in Lithium-argyrodite Solid-State Electrolytes. *npj Comput Mater* **2020**, *6*, 1–10.

(100) Marcolongo, A.; Marzari, N. Ionic Correlations and Failure of Nernst-Einstein Relation in Solid-State Electrolytes. *Phys. Rev. Mater.* **2017**, *1*, 025402.

(101) Eckhardt, J. K.; Kremer, S.; Merola, L.; Janek, J. Heteroionic Interfaces in Hybrid Solid-State Batteries-Current Constriction at the Interface between Different Solid Electrolytes. *ACS Appl. Mater. Interfaces* **2024**, *16*, 18222–18235.

(102) Irvine, J. T. S.; Sinclair, D. C.; West, A. R. Electroceramics: Characterization by Impedance Spectroscopy. *Advanced Materials* **1990**, *2*, 132–138.

(103) Savina, A. A.; Abakumov, A. M. Benchmarking the Electrochemical Parameters of the LiNi0.8Mn0.1Co0.1O2 Positive Electrode Material for Li-ion Batteries. *Heliyon* **2023**, *9*, e21881.